ORIGINAL RESEARCH

Discordant Alternans as a Mechanism for Initiation of Ventricular Fibrillation In Vitro

Laura M. Muñoz, PhD; Anna R. M. Gelzer, Dr. med. vet, PhD; Flavio H. Fenton, PhD; Wei Qian, PhD; WeiYe Lin, BS; Robert F. Gilmour Jr, PhD; Niels F. Otani, PhD

***Background*—**Ventricular tachyarrhythmias are often preceded by short sequences of premature ventricular complexes. In a previous study, a restitution-based computational model predicted which sequences of stimulated premature complexes were most likely to induce ventricular fibrillation in canines in vivo. However, the underlying mechanism, based on discordant-alternans dynamics, could not be verified in that study. The current study seeks to elucidate the mechanism by determining whether the spatiotemporal evolution of action potentials and initiation of ventricular fibrillation in in vitro experiments are consistent with model predictions.

***Methods and Results*—**Optical mapping voltage signals from canine right-ventricular tissue (n=9) were obtained simultaneously from the entire epicardium and endocardium during and after premature stimulus sequences. Model predictions of action potential propagation along a 1-dimensional cable were developed using action potential duration versus diastolic interval data. The model predicted sign-change patterns in action potential duration and diastolic interval spatial gradients with posterior probabilities of 91.1%, and 82.1%, respectively. The model predicted conduction block with 64% sensitivity and 100% specificity. A generalized estimating equation logistic-regression approach showed that model-prediction effects were significant for both conduction block ($P<1\times10^{-15}$, coefficient 44.36) and sustained ventricular fibrillation ($P=0.0046$, coefficient, 1.63) events.

***Conclusions*—**The observed sign-change patterns favored discordant alternans, and the model successfully identified sequences of premature stimuli that induced conduction block. This suggests that the relatively simple discordant-alternans-based process that led to block in the model may often be responsible for ventricular fibrillation onset when preceded by premature beats. These observations may aid in developing improved methods for anticipating block and ventricular fibrillation. **(*J Am Heart Assoc*. 2018;7:e007898. DOI: 10.1161/JAHA.117.007898.)**

Key Words: alternans • arrhythmia (mechanisms) • computer-based model • electrophysiology • ventricular fibrillation

Sudden cardiac death is a leading cause of mortality in the industrialized world, responsible for an estimated incidence of 180 000 to 450 000 deaths annually in the United States.[1] A substantial proportion of sudden cardiac arrests, approximately half in a recent study,[2] are associated with ventricular tachycardia (VT) or ventricular fibrillation (VF). It has been observed clinically that sustained VT and VF are often preceded by several irregularly timed premature complexes,[3,4] and studies conducted to explore this phenomenon have shown that specific coupling interval patterns of premature complexes, such as short-long-short[5] and short-short-short,[6] tend to lead to reentry and VT. Various researchers have examined the mechanism by which premature complexes or pacing history can interact with electrical restitution properties, including the dependence of action potential duration (APD) and conduction velocity (CV) on the preceding diastolic interval (DI) to produce dynamical heterogeneity of refractoriness, wave break, reentry, and VF[7–11] (see elsewhere[12,13] for reviews).

A series of computational studies has been performed to gain insight into the effects of patterns of variable prematurity of ventricular complexes on inducibility of arrhythmias[14–20]; some of these studies[14–18] have employed coupled maps models,[21–26] which are restitution-based computational

From the School of Mathematical Sciences, Rochester Institute of Technology, Rochester, NY (L.M.M., N.F.O.); University of Pennsylvania, Philadelphia, PA (A.R.M.G.); Georgia Institute of Technology, Atlanta, GA (F.H.F.); University of Delaware, Newark, DE (W.Q.); University of Nevada, Las Vegas, NV (W.L.); University of Prince Edward Island, Charlottetown, Prince Edward Island, Canada (R.F.G.).

Accompanying Data S1, Tables S1 through S4, Figures S1 and S2, and Movies S1 through S18 are available at https://www.ahajournals.org/doi/suppl/10.1161/JAHA.117.007898

Correspondence to: Laura M. Muñoz, PhD, School of Mathematical Sciences, Rochester Institute of Technology, 85 Lomb Memorial Dr., Rochester, NY 14623. E-mail: laura.m.munoz@gmail.com

Received March 2, 2018; accepted June 19, 2018.

Clinical Perspective

What Is New?

- This study describes a new in vitro examination of a mechanism for inducing sustained ventricular fibrillation via short sequences of premature ventricular complexes.
- As part of this examination, the predictions of a restitution-based computational model were compared with optical mapping data collected from canine preparations.
- The main novel contribution of the study is a direct and detailed experimental verification of the idea, previously proposed using a relatively simple computer model, that certain sequences of cycle lengths reliably forecast discordant alternans patterns, conduction block, and the development of ventricular fibrillation.

What Are the Clinical Implications?

- This study demonstrates that our computational model is helpful for predicting (1) spatial patterns of discordant alternans, (2) which premature stimulus sequences are more likely to induce conduction block, and (3) which premature stimulus sequences are unlikely to induce ventricular fibrillation.
- This line of research may eventually lead to improved conduction block and ventricular fibrillation forecasting algorithms, along with computational models that identify arrhythmogenic patterns of premature complexes, which could lead to safer antitachycardia pacing strategies for implantable devices.

models that are well suited for rapid simulation of different wave propagation scenarios. Coupled maps models have been used to examine the effects of premature, irregularly timed stimuli on spatial heterogeneity of refractoriness, conduction block formation, and the vulnerable window for block.[14–18] Gelzer et al[27,28] showed that sequences of premature stimuli that were more likely to cause conduction block in a one-dimensional (1D) coupled maps model also predictably induced VF in canine hearts in vivo. It was surprising that this relatively simple 1D restitution model could make such accurate predictions about a process as complicated as the emergence of VF in intact hearts. The remarkable nature of these results led to the present study. We were interested in further investigating the nature of the predictive power of this model—whether the mechanism that led to block in the model could be seen in in vitro experiments, and whether this type of block would lead to VT and VF in these experiments.

Specifically, this study is centered on a hypothesized mechanism for sustained VF induction, in which certain patterns of premature complexes produce discordant alternans (ie, APD alternations that are spatially out of phase with one another), leading to conduction block, reentry, and VF. The results of Gelzer et al[27,28] were consistent with this hypothesized mechanism, but limitations of the in vivo experimental setup made it impossible to determine whether intermediate stages in the mechanism, such as discordant alternans, conduction block, and reentry, were evident, or whether the coupled maps model accurately predicted discordant-alternans patterns or block. In order to further elucidate the mechanism for conduction block and VF, and to examine the accuracy of the coupled maps model, we conducted the present study, in which we tested the in vivo pacing protocols of Gelzer et al[27,28] in canine ventricles in vitro, and recorded the electrical responses using optical mapping methods.

Main Hypotheses

The main stages of the hypothesized mechanism leading to VF, examined here and in Gelzer et al,[27,28] are depicted in the top row of boxes in Figure 1. We note that the in vitro mechanism leading to VF illustrated in Figure 1 is highly simplified, since it omits intermediate stages, such as formation and breakup of spiral waves, along with alternate VF mechanisms, such as triggered activity, which were considered to be outside the scope of the present work. The computational model chosen for this study was a 1D coupled maps model.[18,27,28] When provided with APD and CV restitution data, the model predicts whether a given combination of variable prematurity of stimuli will induce discordant alternans and/or conduction block. As shown in the bottom row of boxes in Figure 1, the model was only capable of explicitly representing the first 3 stages of the in vitro VF mechanism. For this study, we examined certain portions of the mechanism depicted in Figure 1.

Our hypotheses were as follows:

Hypothesis 1 (Alternans-Pattern-Prediction Hypothesis): The computational model will correctly predict in vitro patterns in spatial gradients of APD and DI, including discordant alternans, resulting from the premature complexes.

Hypothesis 2 (Block-Prediction Hypothesis): Sequences of premature stimuli that tend to produce conduction block in the coupled maps model will predictably induce conduction block in vitro.

Hypothesis 3 (VF-Prediction Hypothesis): Sequences of premature stimuli that tend to produce conduction block in the coupled maps model will predictably induce VF in vitro.

Hypothesis 4 (Reentry-Precedes-VF Hypothesis): Instances of sustained VF will be preceded by reentrant waves in vitro.

To aid with recall, the hypotheses are hereafter referred to by their shortened names (eg, Alternans-Pattern-Prediction), rather than their numbers. To evaluate the VF-Prediction Hypothesis, we reproduced the in vivo experiments of Gelzer

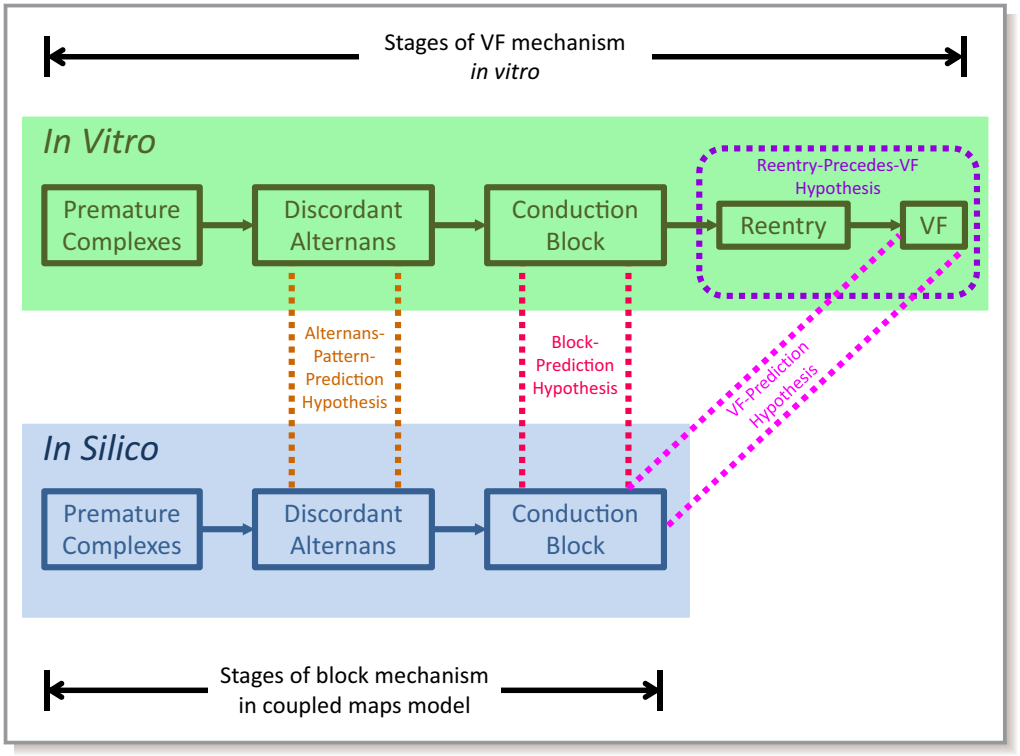

Figure 1. Main stages of the hypothesized mechanism by which premature complexes induce VF. In the top row, premature complexes induce spatially discordant alternans, leading to conduction block, reentrant waves, and VF in vitro. The 1D coupled maps model is capable of simulating the first 3 stages in silico, as shown in the bottom row. Dashed lines indicate pairs of stages that were compared in each of the hypotheses of the study. For instance, the VF-Prediction Hypothesis asserts that there was a relationship between model-predicted block and observed VF (specifically that sequences of premature stimuli that tend to produce block in the model would predictably induce VF in vitro). 1D indicates 1-dimensional; VF, ventricular fibrillation.

et al[27,28] in a new environment (in vitro). Evaluation of the remaining hypotheses, which required acquisition of detailed spatiotemporal AP data, provided new, additional data beyond the work of Gelzer et al.[27,28]

Methods

The data, analytic methods, and study materials will be made available, upon reasonable request, to other researchers for purposes of reproducing the results or replicating the procedure.

Experimental Preparations

Adult beagle dogs (n=9) of either sex were injected with heparin (300 U/kg), and after 10 minutes were euthanized using Fatal-Plus (390 mg/mL pentobarbital sodium, Vortech Pharmaceuticals, 86 mg/kg IV), and their hearts were excised rapidly. The right ventricles (RVs) were cannulated through the circumflex coronary artery with polyethylene tubing, excised, and perfused with normal Tyrode's solution at a rate of 20 mL/min, temperature 37.0±1°C, and perfusion pressure 50 to 80 mm Hg. The preparations, which ranged in size from 4 to 8 cm in length, 4 to 5 cm in width, and 0.5 to 1 cm in depth, were stained with the voltage-sensitive dye di-4-ANEPPS (0.5 μmol/L bolus over 15 minutes), then perfused with blebbistatin (8–40 μmol/L bolus in 500–600 mL Tyrode's solution) until the motion artifact was suppressed. The volume of Tyrode's solution was increased to yield 1 to 5 μmol/L working concentration of blebbistatin in 4L of solution.

Fluorescence emissions were collected simultaneously from the epicardial and endocardial surfaces using two Photometrics Cascade 128+ electron-multiplied charge coupled devices, and the resulting signals (128×128 pixel grid, 500 fps) were recorded using custom-written data collection software. A Fischer Bloom DTU 215A programmable stimulator was used to deliver sequences of rectangular electrical pulses (8–10 mA, 2–10 ms duration) through a bipolar electrode positioned on the endocardial surface of the tissue. APDs, DIs, and conduction block events were

obtained from the endocardial data. This choice was made for consistency with Gelzer et al,[27,28] where monophasic action potentials were collected from the right and left endocardium. In the present study, both endocardial and epicardial data were used to examine the transition from stimulated beats to VF, and to confirm that the preparations were well perfused throughout the experiment.

Pacing Protocols

The pacing protocols used in this study were based on those of the "Group B" experiments in Gelzer et al.[27] In our first protocol, a sequence of 10 S_1 stimuli (cycle length, 500 ms) was applied to the endocardial surface, followed by up to 4 premature stimuli (S_2–S_5). This protocol was designed to (1) identify the effective refractory periods (ERPs) and (2) test whether different combinations of premature stimuli would induce sustained VF (≥30 seconds). To begin to identify the S_2 ERP, a single premature stimulus (S_2) was delivered with an S_1S_2 interval of 250 ms directly after the sequence of 10 S_1 stimuli. The premature stimulus was then delivered at progressively earlier times relative to the 10th S_1 stimulus until S_2 failed to capture. The S_2 ERP was then defined as the minimum S_1S_2 interval at which S_2 captured ($S_1S_{2,min}$). To identify the S_3 ERP, the previous process was repeated after adding an S_3 stimulus, and the size of the S_2S_3 interval was reduced until S_3 failed to capture. S_4 and S_5 ERPs were identified similarly. If alterations were made to the timings of the premature stimuli, for example, if the timing of S_3 was adjusted to change the S_2S_3 interval from $S_2S_{3,min}$ to $S_2S_{3,min}$+50 ms, the values of all subsequent ERPs (S_4 and S_5) were affected and needed to be reidentified.

In the first protocol, interstimulus intervals ending with premature stimuli were categorized as short, intermediate, or long (S, I, or L), as follows. The difference between cycle length (S_nS_{n+1}) and ERP ($S_nS_{n+1,min}$) of the interval between S_n and S_{n+1} was defined as $\Delta S_nS_{n+1}=S_nS_{n+1}-S_nS_{n+1,min}$, for n=1, 2, 3, 4. Each cycle length (CL) that ended with a premature stimulus was classified as short (S), intermediate (I), or long (L), depending on the size of the ΔS_nS_{n+1} value, that is, the amount by which the CL exceeded the ERP. The categories were defined as "S": $0\leq\Delta S_nS_{n+1}\leq5$ ms, "I": $5<\Delta S_nS_{n+1}\leq40$ ms, and "L": $\Delta S_nS_{n+1}>40$ ms. Hence, an S_2–S_5 sequence with $\Delta S_1S_2=5$ ms, $\Delta S_2S_3=50$ ms, $\Delta S_3S_4=0$ ms, $\Delta S_4S_5=2$ ms, belongs to the category SLSS. "X" is a placeholder that refers to an interval of any length, thus XL includes all S_2–S_3 sequences in categories SL, IL, and LL. Different combinations of premature stimulus sequences were applied to the tissue, and it was noted whether any of them induced sustained VF. For each preparation, we attempted to test examples from as many distinct sequence categories as possible, starting with SX and SLSX, and progressing through other sequence categories as time permitted. This sequence search was interwoven with the ERP identification protocol, both due to the need to reidentify ERPs when changes were made to the preceding intervals, and because searching for ERP values automatically led to applying different premature stimulus combinations to the tissue. The complete list of sequences that were tested, along with VF outcomes, is described in Data S1 and shown in Table S1.

The second protocol was a dynamic pace-down protocol used to generate APD-DI restitution data.[29] Sequences of 50 stimuli were delivered to the tissue at a constant cycle length, starting with S_1S_1=600 ms. After each round of 50 stimuli, the cycle length was decreased by 50 ms intervals until S_1S_1=300 ms, by 25 ms intervals until S_1S_1=200 ms, and then by 10 ms intervals until an arrhythmia was induced or 2:1 block occurred.

All experimental procedures were approved by the Institutional Animal Care and Use Committee of the Center for Animal Resources and Education at Cornell University.

Overview of Data Sets and Data Requirements

Three of our hypotheses, specifically the Alternans-Pattern-Prediction, Block-Prediction, and VF-Prediction Hypotheses, made claims about the predictive capabilities of the coupled maps model. Hence, to test these hypotheses, we needed to obtain all required inputs to the model, which included ΔS_nS_{n+1} values, APD versus DI curves (called APD restitution curves), and CV versus DI restitution curves.

To test the Alternans-Pattern-Prediction and Block-Prediction Hypotheses, we restricted our analysis to premature stimulus trials in the SLSS sequence category and nearby categories, that is, SLIX and SLSX. These patterns were of interest because SLSS sequences were shown to be arrhythmogenic in previous studies.[27,28] Due to the large number of steps currently required to process each premature stimulus trial, we randomly selected 18 trials (2 per dog for all 9 dogs) from the SLIX/SLSX group, as opposed to processing all trials, which numbered in the hundreds per dog. Selected trials were confined to recordings where all 5 stimuli (S_1–S_5) captured, to avoid certain trials where a stimulus failed to induce an AP or was preempted by a spontaneous complex. We are using the term *stimulated* complex to refer to an action potential induced by an S_n stimulus, where n = 1, 2, 3, 4, or 5, while *spontaneous* complex refers to a nonstimulated action potential. To test the Alternans-Pattern-Prediction Hypothesis, one additional trial, specifically the second of the 2 trials from the Dog 5 data set, was excluded from the 18 randomly selected trials, due to several missing APD measurements for the premature beats. The missing measurements were caused by incomplete repolarization of the premature APs; that is, the

repolarizations for this trial did not all drop below APD_{50}, which was the threshold chosen for the premature stimulus trials.

To test the VF-Prediction Hypothesis, the main data source, in addition to the restitution curves, was the list of tested premature stimulus sequences and corresponding sustained VF outcomes, which is shown in Table S1. To evaluate the Reentry-Precedes-VF Hypothesis, we used videos of AP propagation across both the endocardial and epicardial surfaces, obtained from 15 recordings where sustained VF followed a sequence of premature stimuli.

Data Analysis

Normalization and averaging

As an initial step, the optical data files were read into a custom-written Java processor.[30] Membrane potential data were indexed by pixel coordinates (*x, y*) in the selected imaging plane (endocardial or epicardial) and by time (*t*). The data were normalized on a scale from 0 to 10 000, then time-averaged using a uniformly weighted 7-step average centered on time *t*, and spatially averaged using a Gaussian-weighted average over a 13×13-pixel grid centered on pixel (*x, y*), with a variance of 2 pixels squared. The normalized and averaged membrane potential value at location (*x, y*) and time *t* was denoted as V(*x, y, t*). All subsequent processing steps were carried out in MATLAB (Mathworks, Natick, MA).

APD computation and determination of APD restitution functions

The recordings contained endocardial and epicardial views of the right ventricles, along with parts of the surrounding heat bath. To exclude the heat bath from the recordings, pixels for which the temporal standard deviation of V(*x, y, t*) fell below a specified threshold were excluded from the data sets. The threshold was adjusted manually for each recording and was typically in the range of 1000 to 3000 in normalized membrane potential units. In cases where this method did not identify the tissue boundary clearly, the dish region was masked out manually. The remaining steps were applied to the endocardial data. Depolarization times were computed as the times at which local maxima of dV_f/dt occurred, where V_f refers to V(*x, y, t*) time-series data that were passed through a zero-phase-shift second-order low-pass Butterworth filter (cutoff frequency=0.15×Nyquist frequency). Filtering was used only at this stage to reduce noise in the dV/dt signals, which facilitated identification of the local maxima. The resting potential between successive APs was computed as the minimum V(*x, y, t*) value between successive depolarization times, except when an AP did not achieve full repolarization, in which case the resting potential following that AP was set equal to the most recent local minimum of V(*x, y, t*) that was preceded by full repolarization. The amplitude of each AP was computed as the difference between its maximum value over time and the preceding resting potential value. Repolarization times were marked at 50% (for premature stimulus data) or 75% (for dynamic pace-down data) of full repolarization and used to compute APD_{50} and APD_{75} values, in milliseconds. For the dynamic pace-down data, APD was modeled as a function of the preceding DI. For each preparation, an APD restitution curve was obtained by performing a nonlinear least squares fit of the function $APD=a+b\ e^{-DI/c}$ to APD and DI values derived from the pixel at the centroid of the endocardial region.

ERP computation

ΔS_nS_{n+1} values (ie, ERPs subtracted from CLs) for S_1–S_5 were required for sorting premature stimulus trials into sequence categories for comparison with VF outcomes. For the 18 randomly selected trials, these values were used as inputs to the coupled maps model. Cycle lengths were imported from laboratory notes or determined from AP emergence times in optical mapping recordings. ERPs, which were measured using the protocol described previously, typically had an uncertainty of −0/+2 ms; for example, if capture was observed at 168 ms but not at 166 ms, then the ERP was known to be >166 ms but ≤168 ms. However, for certain trials, ERP measurements were either unavailable because of the ERP identification protocol being interrupted by an arrhythmia, or had higher uncertainty (≥10 ms) due to infrequent situations, such as ERP values drifting over time, that led us to be less certain of the threshold for capture. We computed averages of low-uncertainty ERP values (organized by sequence category) by drawing from premature stimulus data for all 9 dogs, then used these average values to replace unavailable or highly uncertain ERP measurements.

Determination of APD and DI spatial gradients

For each of the 18 randomly selected trials, we computed $\Delta APD/\Delta x$ (a measure of the spatial gradient of APD) for each AP. To start with, for each of the 9 dogs, we selected $\mathbf{x}_{prox}=(x_{1prox}, x_{2prox})$, a point proximal to the stimulating electrode, and $\mathbf{x}_{dist}=(x_{1dist}, x_{2dist})$, a point distal to the electrode. Both points were chosen on the endocardial surface based on visual inspections of wave front isochrone plots for S_1–S_5. $\mathbf{x}_{prox}$ was chosen near the tip of the stimulating electrode, and $\mathbf{x}_{dist}$ was chosen to lie on the proximal side of the region of wave front slowing (≤10 cm/s), over all trials selected for that dog, that was closest to the center of the tip of the stimulating electrode. The electrode tip was visible in each recording, and its location was estimated visually. The

motivation for this selection method was to identify a span of tissue, bracketed by the proximal and distal points, that was uninterrupted by conduction block. The proximal and distal points were held fixed across trials within each dog but varied from one dog to the next.

To reduce the influence of noise and outliers on our measurements, we chose to first compute median APD values over proximal and distal regions, which we defined as squares, each with side length 0.5 cm. One vertex of the proximal square was anchored to $\mathbf{x}_{prox}$, a vertex of the distal square was anchored to $\mathbf{x}_{dist}$, and the squares were then aligned to avoid overlap with the electrode and with regions of wave front slowing. The spatial gradient of APD was then defined as

$$\Delta APD/\Delta x = (APD_{dist,med} - APD_{prox,med})/|\mathbf{x}_{dist} - \mathbf{x}_{prox}|$$

where $APD_{dist,med}$ and $APD_{prox,med}$ are, respectively, the median APD values over the distal and proximal squares, and $\Delta x=|\mathbf{x}_{dist}-\mathbf{x}_{prox}|$ is the Euclidean distance between $\mathbf{x}_{dist}$ and $\mathbf{x}_{prox}$. $\Delta DI/\Delta x$ was computed similarly. $\Delta APD/\Delta x$ and $\Delta DI/\Delta x$ values were computed from APD_{50} and DI_{50} data. While APD_{75} and DI_{75} would have been preferred to maintain consistency with the dynamic pace-down measurements, the lack of full repolarization on many premature complexes made these quantities difficult to obtain. In future work, extrapolation methods[31] could be explored as an alternative approach for estimating APD_{75}.

Calculation of beat-to-beat changes in APD and DI spatial gradients

We defined $\Delta(\Delta APD/\Delta x)_{S3,S2,i}$ (for i=1, 2, . . ., N) to be the value of $\Delta APD/\Delta x$ measured for stimulus 3 minus the value of $\Delta APD/\Delta x$ for stimulus 2 during the i-th observation out of a total of N, with $\Delta(\Delta APD/\Delta x)_{S4,S3,i}$, and $\Delta(\Delta APD/\Delta x)_{S5,S4,i}$ similarly defined. When $\Delta(\Delta DI/\Delta x)$ was of interest, $\Delta(\Delta DI/\Delta x)_{S3,S2,i}$, $\Delta(\Delta DI/\Delta x)_{S4,S3,i}$, and $\Delta(\Delta DI/\Delta x)_{S5,S4,i}$ were defined analogously.

Identification of conduction block regions

For each of the 18 randomly selected trials, we marked the locations on the endocardial surface, if any, where conduction block occurred. To accomplish this, the CV magnitude at each (*x, y*) point was computed as the reciprocal of the magnitude of the gradient (in seconds per centimeter), computed using the "gradient" function in MATLAB, of the depolarization time at that point. Conduction block was defined as

1. Sufficiently slow speed, meaning a CV magnitude between 0.5 cm/s and 10 cm/s, where the lower bound was included to filter out weakly stained areas at the tissue border, and
2. Visual evidence that the orientation of the wave front isochrones changed direction between the proximal and distal sides of the proposed location of the line of block.

We included the second part of the definition to isolate areas of wave slowing that seemed more likely to be able to induce reentrant behavior. Condition 1 was verified using a MATLAB script that highlighted regions of slow speed on spatial maps of the endocardial surfaces. Condition 2 was verified by visual inspection of activation maps. Examples of conduction block regions are shown in the S_5 AP activation maps in the Results section.

One-Dimensional Coupled Maps Model

We used a 1D coupled maps model, shown in Equations 1 through 3 below, that was previously used by Otani[18] to predict the spatiotemporal evolution of APs resulting from premature stimuli applied at one end of the fiber. Eq. 1 describes the n-th APD as a function of distance x along a 1D fiber of length L, where the stimulus is applied at the left end (x=0), Eq. 2 describes how the n-th basic cycle length (BCL) varies along the fiber due to the effects of CV restitution, and Eq. 3 relates DI, BCL, and APD at distance x_j along the fiber. The APD and CV restitution functions, which are $\alpha(.)$ and v(.) respectively, are given in Table 1. For all simulations, each fiber was discretized into segments of uniform length dx=0.25 cm, where x_j=j dx.

$$APD_n(x_j) = \alpha(DI_{n-1}(x_j)) \quad (1)$$

$$BCL_n(x_j) = BCL_n(0) + \sum_{k=1}^{j-1} \frac{dx}{v(DI_n(x_k))} - \sum_{k=1}^{j-1} \frac{dx}{v(DI_{n-1}(x_k))} \quad (2)$$

$$DI_n(x_j) = BCL_n(x_j) - APD_n(x_j) \quad (3)$$

For each right ventricle, coupled maps model simulations were conducted using APD restitution and DI_{min} (the minimum DI value measured during the dynamic pace-down protocol) parameters calibrated to dynamic pace-down data obtained from that ventricle, along with CV restitution parameters (other than DI_{min}) based on those of Gelzer et al.[27,28] Values and/or sources for the parameters are listed in Table 1.

Gelzer et al[27,28] computed APD restitution curves from their monophasic action potential data, but obtained the non-DI_{min} CV restitution parameters from a different study by Riccio et al,[32] in which CV was measured in beagle myocardium. Gelzer et al had no means of measuring CV in

Table 1. Parameter Values for Coupled Maps Model Simulations

Parameter Name	Parameter Setting or Source
Fiber length	7 cm
Spatial step size, dx	0.25 cm
APD restitution parameters a, b, c $APD=\alpha(DI)=a+b\ e^{-DI/c}$ in ms	Obtained from curve fit to pace-down data (1 set of values per right ventricle)
DI_{min}	Minimum DI, in milliseconds, measured during pace-down (1 value per right ventricle)
Parameters from restitution function $CV=v(DI)=72\left(1-e^{-(DI-DImin+34.82)/28.0}\right)$ in cm/s	Version used by Gelzer et al[27,28] modified to be consistent with typical measurements of DI_{min}

APD indicates action potential duration; CV, conduction velocity; DI, diastolic interval.

their in vivo setup; hence, it was essential for them to obtain CV restitution curves from a different source. In our study, we aimed to make our prediction methods similar to those of Gelzer et al in order to make a fairer comparison with their results; therefore, we obtained APD restitution curves from our optical data but used CV restitution curve parameters based on those of Riccio et al.[32] In accordance with Gelzer et al, we adjusted one CV restitution parameter, DI_{min}, to match the value observed in each ventricle.

To test the Alternans-Pattern and Block-Prediction Hypotheses, for each of the randomly selected premature stimulus trials, a corresponding coupled maps simulation was performed in MATLAB with premature stimulus timings that matched the in vitro ΔS_nS_{n+1} values. From these simulations, we recorded values of $\Delta APD/\Delta x$ and $\Delta DI/\Delta x$, along with the location of conduction block, if any. For the coupled maps model simulations, the spatial APD gradient was defined as:

$$\Delta APD/\Delta x = (APD(x_{dist}) - APD(x_{prox}))/|x_{dist} - x_{prox}|$$

Here, x_{prox} was fixed at the left (stimulated) end of the fiber, and $|x_{dist}-x_{prox}|$ was set to the smallest of the following quantities: the fiber length, the distance between the left end of the fiber and block (if any occurred), or the Δx value used in the corresponding in vitro trial. There was no need to take medians of APD values since the simulations were fully deterministic. $\Delta DI/\Delta x$ was computed in a similar fashion.

To test the VF-Prediction Hypothesis, simulations of hundreds of thousands of combinations of premature stimuli were performed, covering 1 to 4 premature stimuli, and testing all possible combinations of CL − ERP (ie, ΔS_nS_{n+1}) values in the range of 0 to 70 ms, in increments of 1 ms, for each interstimulus interval. For each stimulus sequence tested in this manner, the block outcome (ie, whether block occurred) was recorded. Conduction block was treated as an indicator of the overall arrhythmogenic potential of a sequence: if ≥25% of the tested sequences in a category (eg, SS) yielded block in simulations, then that category was classified as being likely to produce VF in vitro.

Statistical Analysis

To test the Alternans-Pattern-Prediction Hypothesis, which asserts that the model will correctly predict in vitro spatial gradients of APD and DI, we focused on beat-to-beat changes in sign of these quantities. For the randomly selected trials, the possibility that $\Delta(\Delta APD/\Delta x)$ or $\Delta(\Delta DI/\Delta x)$ alternate in sign, specifically that they follow a discordant-alternans (−, +, −) pattern, was evaluated using a Bayesian statistical approach. Values of $\Delta(\Delta APD/\Delta x)$ or $\Delta(\Delta DI/\Delta x)$ for the three pairs of adjacent complexes (S_2–S_3, S_3–S_4, and S_4–S_5) were formed into length-3 vectors $\mathbf{y}_i$, i=1, 2,. . ., N. Here, i is the index of the observation, and d=3 is the number of elements in each vector $\mathbf{y}_i$; for example, when analyzing APD spatial gradients, the elements of $\mathbf{y}_5$ are the 3 sequential values of $\Delta(\Delta APD/\Delta x)$ observed in the fifth trial in the set of randomly selected trials. We assumed that the $\mathbf{y}_i$'s were independently generated by a Gaussian distribution with mean $\boldsymbol{\mu}=(\mu_1, \mu_2, \mu_3)^T$ and precision matrix $\boldsymbol{\Lambda}$. A classic noninformative prior known as the independence Jeffrey's prior[33,34] was chosen for $(\boldsymbol{\mu}, \boldsymbol{\Lambda})$ with density function

$$p(\boldsymbol{\mu}, \boldsymbol{\Lambda}) \propto (\det\boldsymbol{\Lambda})^{-\frac{d+1}{2}}$$

By applying Bayes' theorem, $p(\boldsymbol{\mu}, \boldsymbol{\Lambda}|\mathbf{x}) \propto p(\mathbf{x}|\boldsymbol{\mu}, \boldsymbol{\Lambda})\ p(\boldsymbol{\mu}, \boldsymbol{\Lambda})$, where $\mathbf{x}$ represents the set of N observations $\mathbf{y}_1, \mathbf{y}_2, \ldots, \mathbf{y}_N$, the posterior distribution of $(\boldsymbol{\mu}, \boldsymbol{\Lambda})$ is known to be a normal-Wishart distribution. More precisely, the posterior distribution may be expressed in the following categorical form

$$\boldsymbol{\mu}|\boldsymbol{\Lambda}, \mathbf{x} \sim \text{Gaussian}\left(\bar{\mathbf{y}}, \frac{\boldsymbol{\Lambda}^{-1}}{N}\right)$$

$$\boldsymbol{\Lambda}|\mathbf{x} \sim \text{Wishart}(\mathbf{S}^{-1}, N)$$

where $\bar{\mathbf{y}} = (1/N)\Sigma_{i=1}^{N}\mathbf{y}_i$ and $\mathbf{S} = \Sigma_{i=1}^{N}(\mathbf{y}_i - \bar{\mathbf{y}})(\mathbf{y}_i - \bar{\mathbf{y}})^T$. Integrating the posterior distribution over the entire domain of the precision matrix $(\boldsymbol{\Lambda})$ leads to the posterior marginal density function for $\boldsymbol{\mu}$:

$$p(\boldsymbol{\mu}|\mathbf{x}) \propto [1 + N(\boldsymbol{\mu} - \bar{\mathbf{y}})^T\mathbf{S}^{-1}(\boldsymbol{\mu} - \bar{\mathbf{y}})]^{-N/2}$$

which is known to be a multivariate *t*-distribution.

The posterior distribution $p(\boldsymbol{\mu}|\mathbf{x})$, regarded as a function of $\boldsymbol{\mu}$, was then integrated over each of the 8 coordinate-axis-

defined octants, yielding the posterior probability that $\boldsymbol{\mu}$ (ie, the population vector means of $\Delta(\Delta APD/\Delta x)$ or $\Delta(\Delta DI/\Delta x)$) would have the set of signs associated with that octant. Each octant covers one of the 8 possible sequences of arithmetic signs, including (+, +, +), (−, −, −), (−, +, −), etc. The integration was carried out by applying Simpson's rule in all 3 directions using 101 grid points in each direction. The sum of these 8 probabilities was also checked to see if it was close to 1.0 to within acceptable error. The posterior probabilities for APD and DI gradient changes are given the Results section, with further detail provided in Tables S2 and S3. To help visualize the posterior distribution, the contour plots of the posterior marginal density functions for (μ_1, μ_2), (μ_2, μ_3) and (μ_1, μ_3) [denoted by $p(\mu_1, \mu_2|\mathbf{x})$, $p(\mu_2, \mu_3|\mathbf{x})$ and $p(\mu_1, \mu_3|\mathbf{x})$, respectively] were also created and are shown in Figures S1 and S2. MATLAB was used for these computations.

To test the Block-Prediction Hypothesis, we examined the coupled maps model's ability to predict conduction block instances that were observed in the optical data, by tallying simulated and observed block occurrences in a 2×2 table. While we considered using Fisher's exact test to test the hypothesis, we instead chose to apply a Wald test to a generalized estimating equation (GEE) logistic regression model, where the GEE model incorporates clustering by dog, to appropriately control for the dependence of observations on dogs. In the GEE model, the binary dependent variable was the occurrence of measured conduction block and the binary explanatory variable was the occurrence of simulated block. The comparisons between predicted and measured block were limited to block on the S_5 wave front because, for the randomly selected trials, the model did not predict any instances of block on S_1–S_4 (this was a consequence of our choice to sample only from sequence categories near SLSS, for which the model is highly unlikely to predict block on S_1–S_4).

To test the VF-Prediction Hypothesis, we indexed each in vitro test of a stimulus sequence category (such as SLSS) by (1) the dog; (2) model prediction, ie, whether ≥25% or <25% of the combinations of stimulus timings in that category produced block in simulations of the coupled maps model; and (3) outcome, ie, whether sustained VF was induced in vitro. Next, we analyzed the data using 2 different statistical methods to determine the significance of the association between the coupled maps predictions and the in vitro VF outcomes. In the first method, which was based on the statistical approach of Gelzer et al,[27,28] we used JMP (SAS Institute Inc., Cary, NC) to apply an effect likelihood ratio test to a logistic regression model of sustained VF responses, where the sustained VF outcome was the binary dependent variable, and the explanatory variables were the binary (≥25% or <25%) coupled maps model prediction and the dog index (1–9). This approach was included in this study to allow direct comparisons of our results with those of Gelzer et al.[27,28] In the second statistical method, a Wald test was applied to a GEE logistic regression model, with sustained VF outcome as the binary dependent variable, and coupled maps prediction as the binary explanatory variable, with clustering by dog. The GEE-based method is considered to be more reliable than the first method because the GEE approach controls more appropriately for the dependence of observations on dogs. All GEE logistic regression models used in this study were constructed and analyzed in R (R Foundation for Statistical Computing), using logit.gee within the zelig package.[35–37] For all statistical tests, a value of $P<0.05$ was considered statistically significant.

Classification of Sign Patterns

To aid in the analysis of the Alternans-Pattern-Prediction Hypothesis, we sorted the randomly selected trials according to whether they showed good, intermediate, poor, or inverse agreement with the model-predicted sequence of signs of beat-to-beat changes in spatial gradients of APDs and DIs. The model-predicted sequence of signs was (−, +, −) for $(\Delta(\Delta APD/\Delta x)_{S3,S2}, \Delta(\Delta APD/\Delta x)_{S4,S3}, \Delta(\Delta APD/\Delta x)_{S5,S4})$ for the all of the randomly selected trials. The coupled maps model predicted the same sequence of signs for the $\Delta(\Delta DI/\Delta x)$ quantities for the selected trials. Separate sets of agreement scores, one for $\Delta(\Delta APD/\Delta x)$ sequences, and another for $\Delta(\Delta DI/\Delta x)$ sequences, were computed according to the following definitions. "Good" agreement was defined as 3 out of 3 measured signs (for example, for a sequence of $\Delta(\Delta APD/\Delta x)$ values) matching the model-predicted signs; that is, both the measured and model-predicted sign sequences were (−, +, −). "Intermediate" agreement was defined as 2 of 3 measured signs matching the predicted elements in the sign sequence; for example, an observed sequence of (−, +, +) would fit into the "intermediate" category because the first 2 elements match the model-predicted signs. "Poor" agreement was defined as only one of the measured signs matching its model-predicted counterpart; for example, (+, −, −) has poor agreement because only the last element matches with its predicted sign. The "inverse" category was defined as (+, −, +), in which each measured sign was the opposite of its model-predicted counterpart. We checked the indexing of the APDs and DIs to ensure that any sequences in the "inverse" category were not the result of a mistake (eg, a 1-step offset) in indexing of the APs.

Assessment of Reentry

To assess the Reentry-Precedes-VF Hypothesis, a qualitative visual review was performed of the 15 recordings (not limited to the randomly selected trials) where sustained VF followed a sequence of premature stimuli. This review consisted of

watching the corresponding movies of AP progression and examining the events following the stimulated complexes. We made note of behavior that appeared to be consistent with reentry, such as wave front slowing of the final stimulated AP, followed by a shift in the direction of propagation, along with any behavior that did not appear to be reentrant, such as focal spontaneous complexes that emerged directly after the stimulated complexes. To illustrate our classification process further, examples of focal complexes and reentrant behavior are shown in the 2-dimensional spatial membrane potential images in the Results section. Movies of AP propagation from premature stimulus trials are shown in Movies S1 through S18, of which, Movies S3 and S5–S18 correspond to the recordings of sustained VF that were observed to follow sequences of premature stimuli.

Results

Optical Mapping Data

Examples of activation maps showing S_1 AP wave front arrival times are given in Figure 2. One activation map is shown for each of the 9 endocardial surfaces, where the maps were obtained from the randomly-selected trials that were used to test the Alternans-Pattern-Prediction and Block-Prediction Hypotheses. There were 2 to 3 S_1 APs recorded during each of the randomly selected trials, and a representative S_1 activation map is shown for each of the 9 right ventricles. These maps are provided to show the response to slow pacing for each of the ventricles, before the S_2 to S_5 stimuli were applied. Due to the length of the S_1S_1 interval (500 ms), the S_1 AP propagation was expected to be relatively uniform, compared with the propagation of the S_2 to S_5 APs. The S_1 AP propagation was relatively uniform for Dogs 1 to 8, but the wave front shapes were more complicated for Dog 9, as shown in Figure 2I, which includes an interior region of block that appears as a yellow spot surrounded by black border. Examination of the records for Dog 9 has not revealed any clear differences in anatomy, experimental conditions, or tissue health that would explain its more complex S_1 AP propagation.

Agreement Scores for Discordant Alternans Sign Patterns

The percentages of randomly selected trials that fit into each of the 4 categories (good, intermediate, poor, and inverse) for discordant alternans sign patterns are shown in Table 2. The first row of Table 2 contains agreement scores for $\Delta(\Delta APD/\Delta x)$ patterns. The second row gives percentages corresponding to predictions for $\Delta(\Delta DI/\Delta x)$. Table 2 shows that the majority of trials [64% for $\Delta(\Delta APD/\Delta x)$ and 82% for $\Delta(\Delta DI/\Delta x)$] had either good or intermediate agreement with the model-predicted sign patterns.

Detailed Comparisons of Predictions With Observations

In this section, we show detailed comparisons of selected trials with the stages of the theorized VF mechanism. Membrane potential time-series data from 4 trials, labeled Trial NB, Trial 1, Trial VF, and Trial 2, where NB stands for "no block," are shown in Figure 3A through 3D. Each of these trials corresponded to a test of a premature stimulus sequence in the SLSX category. Specifically, these trials are examples of outcomes from our S_4S_5 ERP identification protocol, where we had already identified ERPs for S_1S_2, S_2S_3, and S_3S_4, were holding S_1S_2, S_2S_3, and S_3S_4 constant in an SLS pattern, and were in the process of searching for the S_4S_5 ERP through successive reductions of S_4S_5. This resulted in a progression from SLSL to SLSI, with an intended destination of SLSS.

These 4 trials are of interest because they cover a range of levels of agreement and disagreement with model predictions, where one sequence of trials (Trials NB, 1, and VF) initially showed good agreement with model predictions, leading to the anticipated outcome of sustained VF, whereas the remaining trial (Trial 2) initially showed poor agreement with model predictions, and was part of a sequence of trials that did not lead to the anticipated outcome of sustained VF. In making these selections, we favored trials that were members of the randomly selected set of trials chosen for statistical analyses of discordant alternans and conduction block outcomes. The main settings and features of the four trials are summarized below, and the corresponding observations and model predictions for these trials are listed in Table 3.

1. Trial NB: This was a test of an SLSL sequence on the RV of Dog 4, with (S_1S_2, S_2S_3, S_3S_4, S_4S_5)=(160, 160, 102, 170) ms. This trial received "good" agreement scores for both APD and DI-based discordant alternans sign patterns. The coupled maps model predicted that no S_5 conduction block would occur, and conduction block was not observed in vitro. Hence, the trial was fully consistent with the model's predictions for both discordant alternans and block. As seen in Figure 3A, the S_5 AP was followed by nine spontaneous complexes (ie, APs that occurred spontaneously rather than being induced directly by stimuli). Based on the corresponding movie of AP propagation (Movie S1), the complexes were judged to be focal in nature; the process used for distinguishing focal complexes from reentrant waves is illustrated in more detail later in this section. After the ninth spontaneous complex, no further activity was observed, and VF was not induced.

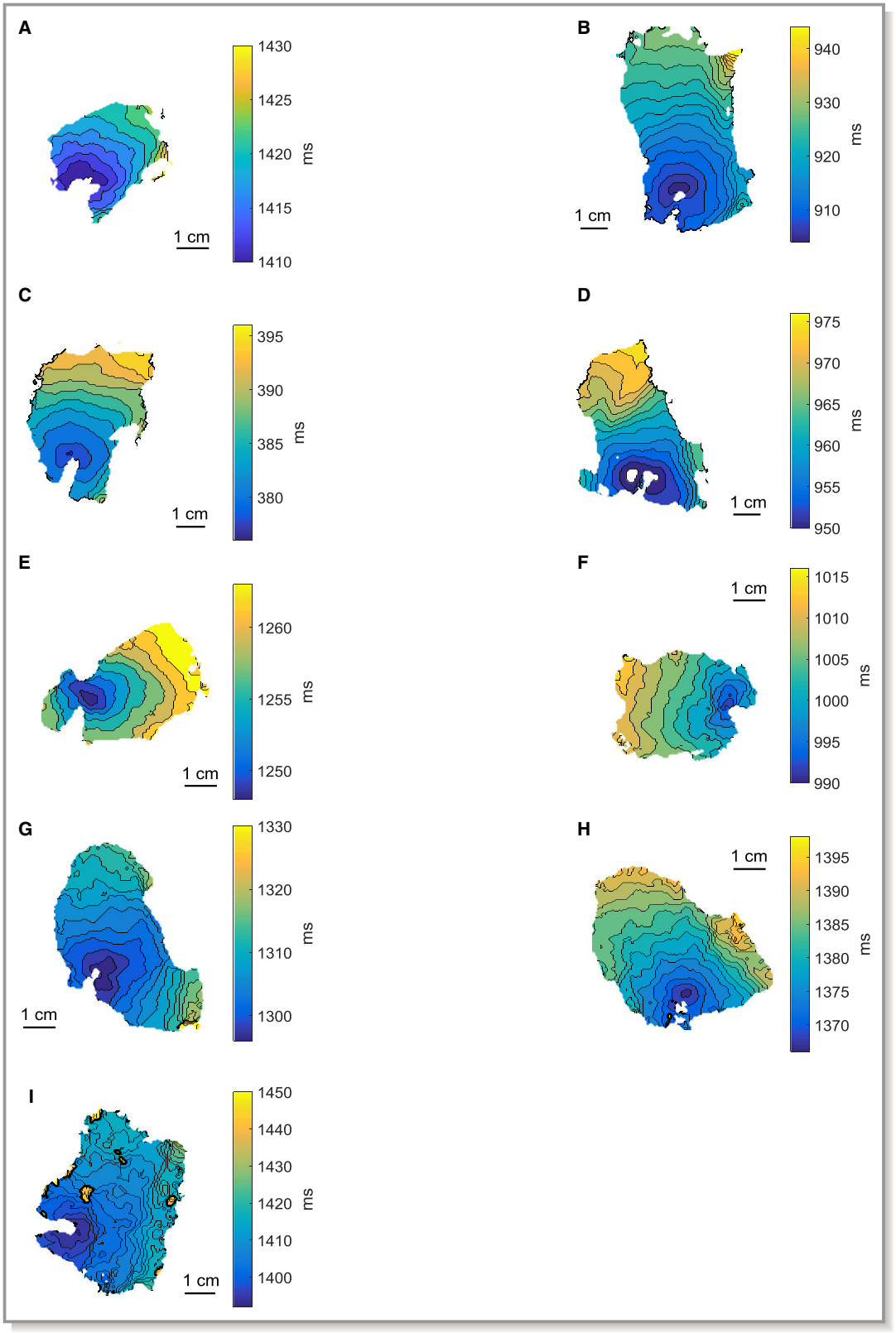

Figure 2. Activation maps of S_1 APs for Dogs 1 through 9. Each 2-dimensional map shows activation times (in milliseconds) measured on the endocardial surface for an S_1 AP. Each map was obtained from one of the 18 randomly selected trials that were used to test the Alternans-Pattern-Prediction and Block-Prediction Hypotheses. A, B, . . ., I correspond to Dogs 1, 2, . . ., 9, respectively. AP indicates action potential.

Table 2. Model-Agreement Scores for Beat-to-Beat Changes in APD and DI Spatial Gradients

Quantity	Good (3/3)	Intermediate (2/3)	Poor (1/3)	Inverse (0/3)
$\Delta(\Delta APD/\Delta x)$	40%	24%	18%	18%
$\Delta(\Delta DI/\Delta x)$	35%	47%	18%	0%

APD indicates action potential duration; DI, diastolic interval.
The first row contains the percentages of premature stimulus trials that fell into each category of agreement (good, intermediate, poor, or inverse) with the sequence of signs predicted for $\Delta(\Delta APD/\Delta x)$ by the coupled-maps model. For example, for a trial in the "good" category, the signs of all 3 elements in the measured $(\Delta(\Delta APD/\Delta x)_{S3,S2}, \Delta(\Delta APD/\Delta x)_{S4,S3}, \Delta(\Delta APD/\Delta x)_{S5,S4})$ list of values matched with the model-predicted discordant alternans pattern of (−, +, −). Trials in the "intermediate," "poor," and "inverse" categories had, respectively, 2, 1, or 0 measured signs that matched with the model-predicted signs. The second row gives percentages corresponding to predictions for $\Delta(\Delta DI/\Delta x)$.

2. Trial 1: After Trial NB was recorded, the S_4S_5 interval was reduced in 2-ms steps, eventually leading to Trial 1, which was a test of an SLSI sequence on the RV of Dog 4, with (S_1S_2, S_2S_3, S_3S_4, S_4S_5)=(160, 160, 102, 134) ms. This trial received "good" agreement scores for both APD and DI-based discordant alternans sign patterns. The coupled maps model predicted that S_5 conduction block would not occur, yet conduction block was observed in vitro. As seen in Figure 3B, the S_5 AP was followed by eight spontaneous complexes, which were classified as focal, based on our review of Movie S2. After the spontaneous complexes, no further activity was observed, and VF was not induced.
3. Trial VF: After Trial 1 was recorded, the S_4S_5 interval was reduced in 2-ms steps, leading to Trial VF, which was a test of an SLSI sequence on the RV of Dog 4, with (S_1S_2, S_2S_3, S_3S_4, S_4S_5)=(160, 160, 102, 120) ms. This trial received "good" agreement scores for both APD and DI-based discordant alternans sign patterns. The coupled maps model predicted that S_5 conduction block would not occur, yet conduction block was observed in vitro. As seen in Figure 3C, the S_5 AP was followed by VF, and a review of the corresponding movie (Movie S3) showed evidence of reentry preceding VF. Unlike Trials NB, 1, and 2, Trial VF was not a member of the set of 18 randomly selected trials used for statistical analyses of alternans and block predictions, but data from Trial VF are shown here to provide an example of sustained VF induction.
4. Trial 2: This was a test of an SLSI sequence on the RV of Dog 9, with (S_1S_2, S_2S_3, S_3S_4, S_4S_5)=(184, 190, 148, 110) ms. This trial received "poor" agreement scores for both APD and DI-based discordant alternans sign patterns. The coupled maps model predicted that S_5 conduction block would occur, and conduction block was observed in vitro. As seen in Figure 3D and Movie S4, no further activity was observed after the S_5 AP, and VF was not induced.

For Dog 4 (the source of Trials NB, 1, and VF), successive reductions of S_4S_5 eventually led to sustained VF. For Dog 9 (the source of Trial 2), sustained VF after SLSI was induced in an earlier trial with (S_1S_2, S_2S_3, S_3S_4, S_4S_5)=(184, 190, 144, 110) ms, and the corresponding VF induction is given in Movie S18. After testing different combinations of stimulus sequences, such as SL and SLS, on the RV of Dog 9, we returned to the SLSI category, during which Trial 2 was recorded, but we were unable to replicate the sustained VF induction that was observed earlier in the experiment, although reducing S_4S_5 in trials subsequent to Trial 2 sometimes yielded spontaneous complexes or non-sustained VF (data not shown).

Comparison of Trial 1 and Trial 2

Trials 1 and 2 were chosen for a head-to-head comparison, since they both belonged to the SLSI category, but were very different in their degrees of agreement with model-based predictions of discordant alternans. The corresponding model-predicted and measured $\Delta APD/\Delta x$ and $\Delta DI/\Delta x$ quantities, plotted against stimulus index (S_1–S_5), are shown in Figure 4. Trial 1 (Figure 4A and 4B), which was a member of the "good" agreement category for discordant alternans patterns, yielded relatively good agreement between the model-predicted and measured sign patterns of APD and DI spatial gradients, while the second trial (Figure 4C and 4D), which was a member of the "poor" agreement category, showed comparatively poor agreement between predicted and observed patterns.

To explore in more detail the "good" and "poor" trial examples in Figure 4, the S_2–S_5 activation maps from Trials 1 and 2 are given in Figure 5. In each plot, the green square surrounds the proximal region, while the red square surrounds the distal region. The distal region selection was constrained by the need to find a proximal-to-distal span that was uninterrupted by conduction block, since the coupled maps model predicts wave behavior up to the point of block within a 1D fiber, but does not make any predictions in locations distal to the block site. Locations of conduction block (as defined in the Methods section) of the S_5 AP wave front that occurred close to the electrode are indicated with pink arrows in Figure 5D and 5H.

Notable distinctions between the activation maps for Trials 1 and 2 include the greater number of instances of conduction block in Trial 2, along with the shorter distance between the proximal and distal locations in Trial 2. Possible reasons for the discrepancies in the degrees of agreement with model predictions are explored further in the Discussion section.

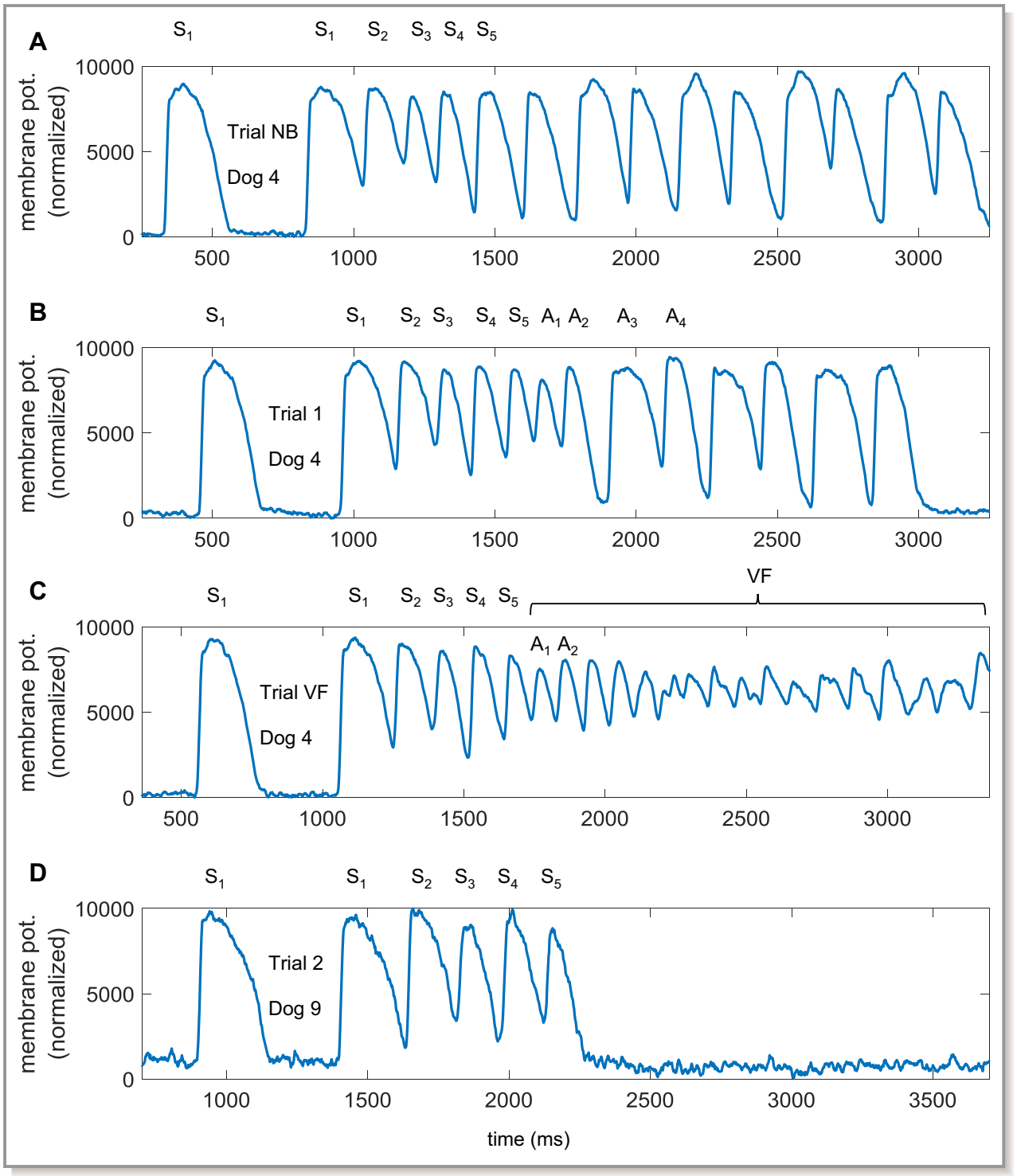

Figure 3. Time-series optical data. In each subplot, membrane potential (dimensionless, normalized to a scale of 0 to 10 000) is plotted against time (milliseconds), for a pixel with coordinates near the center of the field of view on the endocardial surface. Stimulated APs are labeled S_1, S_2, etc. The remaining APs were not stimulated. Several of these nonstimulated APs (ie, spontaneous complexes) are labeled A_1, A_2, etc, for later reference. A, SLSL stimulus trial (Trial NB) recorded from pixel with coordinates (60, 60) in RV of Dog 4. The stimulus sequence was not predicted to cause block, and sustained VF did not occur in vitro. B, SLSI stimulus trial (Trial 1) recorded from pixel with coordinates (60, 60) in RV of Dog 4. The stimulus sequence was not predicted to cause block, and sustained VF did not occur in vitro. C, SLSI stimulus trial (Trial VF) recorded from pixel (60, 60) in RV of Dog 4. The stimulus sequence was not predicted to cause block, and sustained VF occurred in vitro. D, SLSI stimulus trial (Trial 2) recorded from pixel (70, 70) in RV of Dog 9. The stimulus sequence was predicted to cause block, and sustained VF did not occur in vitro. AP indicates action potential; RV, right ventricle; VF, ventricular fibrillation.

Table 3. Summary of Experimental and Model-Predicted Outcomes for Selected Trials

	Discordant Alternans Sign Pattern	S_5 AP Conduction Block	Reentry	VF
Dog 4				
Trial NB (SLSL)				
Experimental outcome	Y	N	N	N
Model prediction	Y	N	N/A	N/A
Trial 1 (SLSI)				
Experimental outcome	Y	Y	N	N
Model prediction	Y	N	N/A	N/A
Trial VF (SLSI)				
Experimental outcome	Y	Y	Y	Y
Model prediction	Y	N	N/A	N/A
Dog 9				
Trial 2 (SLSI)				
Experimental outcome	N	Y	N	N
Model prediction	Y	Y	N/A	N/A

AP indicates action potential; NB, no block; VF, ventricular fibrillation.
"Y" indicates that the corresponding experimental outcome (eg, the discordant alternans (–, +, –) sign pattern) was observed in vitro, or that the model predicted that the outcome would occur. "N" indicates that the outcome was not observed in vitro, or was not predicted to occur by the model. Certain entries are labeled N/A (not applicable), since the model cannot directly represent reentry or VF.

Comparisons of Trials NB, 1, and VF

Trials NB, 1, and VF were members of a sequence of trials that eventually led to sustained VF in the RV of Dog 4. As described previously, the stimulus timings up through S_4 were the same for these trials, but each trial had a different S_4S_5 interval. The corresponding spatial gradients of APD, along with the S_5 activation maps, are shown in Figure 6. For convenience in making comparisons, the APD and S_5 activation time data from Trial 1, previously shown in Figures 4A and 5D, are reproduced in Figure 6B and 6E, respectively. All 3 trials met the criteria for the "good" category of agreement with predicted discordant alternans sign patterns, and from Figure 6A through 6C, it can be seen that the predicted and observed APD spatial gradients were similar for all 3 trials. Figure 6E and 6F show that conduction block occurred in vitro after S_5 in Trials 1 and VF, and that in Trial VF, there were a number of additional regions of block that appeared in the region near the electrode. The model correctly predicted the absence of block of the S_5 AP wave front in Trial NB but failed to predict the S_5 AP block that was observed in Trials 1 and VF. The incorrect block prediction observed in Trials 1 and VF appeared to be part of a larger trend, where the model tended to underpredict conduction block, in general. This tendency is explored further in our statistical analysis of block and the related portion of the Discussion section.

In Trial NB and Trial 1, the S_5 AP was followed by spontaneous activity, seen in Figure 3A and 3B. The spontaneous activity seen in Trial 1 is contrasted with the reentrant behavior witnessed in Trial VF in Figures 7 and 8. A visual review of frames, shown in Figure 7, from the Trial 1 movie (Movie S2) indicated that the 8 spontaneous complexes in Trial 1 appeared to be focal in nature, in the sense that they appeared to originate from a localized region on the endocardium, rather than from the S_5 AP reentering previously activated tissue. Examples of these localized regions are shown in Figure 7C and 7E, where complexes A_1 and A_2 were seen to emerge, and in Figure 7G through 7J, where the emergence locations of complexes A_3 and A_4 are shown. The 9 spontaneous complexes that were observed after the S_5 AP in Trial NB were very similar to the A_3 and A_4 complexes in Figure 7G through 7J. The initial time, t=0 ms, for Figures 7 and 8, as well as for Movies S2 and S3, corresponds to t=800 ms in the time-series plots (Figure 3B and 3C), since the movie start times were offset to begin shortly before the final S_1 AP.

Reentry was observed before VF in Trial VF. The initiation of reentry after S_5 is shown in Figure 8. Figure 8C shows that the S_5 wave back moved away from the electrode, while a spontaneous complex, labeled A_1, appeared near the location marked with a blue asterisk. A spontaneous complex, labeled A_2, emerged from the A_1 AP and propagated into the region near the electrode (Figure 8E), and a portion of the A_2 wave front encountered slow conduction near the region marked with a pink "x" (Figure 8G). After activating the region of slow conduction, a portion of the A_2 AP reentered the region near the electrode (Figure 8I), where the reentrant wave front is labeled with an "R." After the events shown in this figure, another cycle of reentry, similar to the process shown in Figure 8G and 8I, was observed, followed by increasingly disorganized propagation and VF. A movie of optical mapping recordings for Trial VF, showing the evolution of the S_1–S_5 APs followed by reentry and VF, is included in Movie S3. The observed sequence of events (discordant APD alternation, block, reentry, VF) in Trial VF was fully consistent with the in vitro mechanism in the top row of Figure 1.

Converting the SLSI stimulus sequence from the nonarrhythmogenic combination used in Trial 1 to the VF-inducing combination in Trial VF was a simple matter of reducing the S_4S_5 interval, but other, more complex patterns of agreement and disagreement with the theorized VF mechanism were observed, for example in Trial 2, which showed block but no evidence of discordant alternans or reentry.

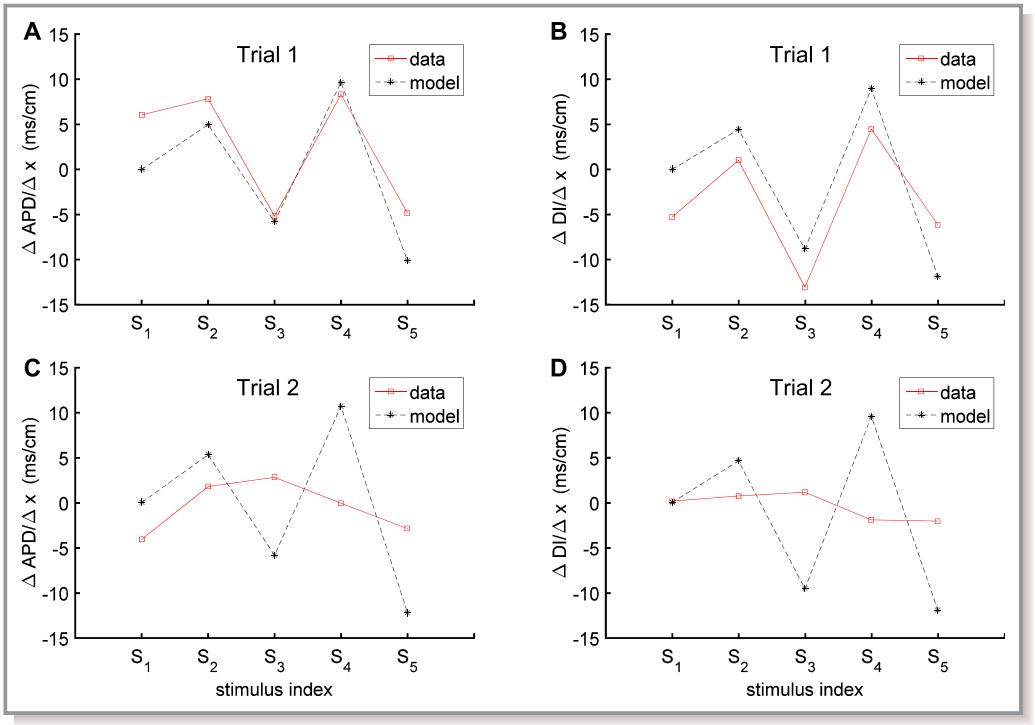

Figure 4. ΔAPD/Δx and ΔDI/Δx vs stimulus index for Trials 1 and 2. Black dashed lines with asterisks indicate model-predicted values, and red solid lines with squares represent measured values. A and B, An example of good agreement between modeled and measured values, from an SLSI stimulus sequence applied to the RV of Dog 4. C and D, An example of poor agreement, from an SLSI stimulus sequence applied to the RV of Dog 9. APD indicates action potential duration; DI, diastolic interval; RV, right ventricle.

Hypothesis Testing

We conducted analyses to test each of our 4 hypotheses, to determine to what extent, if any, the predicted phenomena were present in the data. To test the Alternans-Pattern-Prediction Hypothesis, we measured spatial gradients of APD and DI in each of the randomly selected premature stimulus trials and compared the results with values simulated with the coupled maps model. The coupled maps model predictions shown in Figure 4 suggest that differences in ΔAPD/Δx and ΔDI/Δx for successive stimuli alternate in sign. That is, the coupled maps model predicted that the signs of both Δ(ΔAPD/Δx) and Δ(ΔDI/Δx) should follow a discordant-alternans (−, +, −) pattern. To evaluate this tendency, we used the Δ(ΔAPD/Δx) and Δ(ΔDI/Δx) data to calculate posterior probability distributions of the means of these quantities under the assumed Gaussian distribution. These distributions were then used to determine the posterior probabilities for all possible sequences of signs of the means of Δ(ΔAPD/Δx) and Δ(ΔDI/Δx) for S_3 relative to S_2, S_4 relative to S_3, and S_5 relative to S_4, with the expectation that the predominantly likely sequences should alternate. We found that, for the Δ(ΔAPD/Δx) data, the (−, +, −) pattern of signs was most likely, with a posterior probability of 91.1%. All other sequences of signs had posterior probabilities of less than 6%. For the Δ(ΔDI/Δx) data, the most likely sequence was again (−, +, −), with a posterior probability of 82.1%. The next most likely sequence was (−, +, +) with a posterior probability of 17.3%. All other sequences had posterior probabilities of less than 0.4%. These results may be compared to 12.5% (=1/8), which is the prior probability for all 8 possible sequences if no data were available and no pattern of signs were present. A complete listing of probabilities for all possible sign patterns, along with contour plots of the probability density functions, are given in Tables S2 and S3 and Figures S1 and S2.

To test the Block-Prediction Hypothesis, we tallied the occurrences of model-predicted and experimentally observed conduction block that occurred on S_5 wave fronts for each of the 18 randomly selected trials. The results are summarized in Table 4. The sensitivity and specificity were 64% and 100%, respectively. A Wald test applied to the GEE logistic regression model of conduction block, with clustering by dog, showed that the effect of the coupled maps model prediction of block was significant ($P<1\times10^{-15}$), with a regression coefficient estimate of 44.36 and standard error 0.76. The scale parameter estimate was 0.5, with a standard error of 0.15.

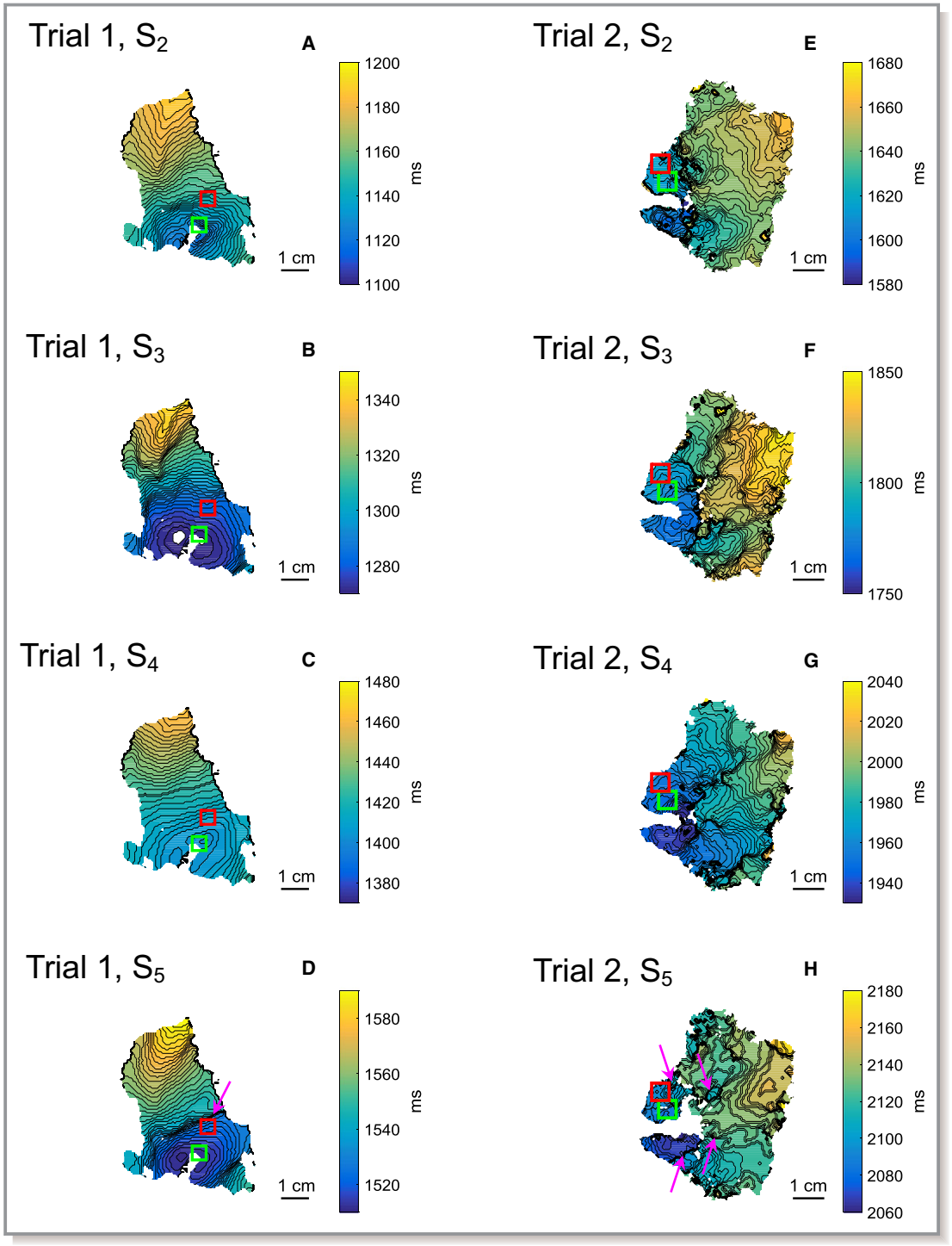

Figure 5. Activation maps for S_2–S_5 APs for Trials 1 and 2. Endocardial activation times (in milliseconds) are shown for Trial 1 from Dog 4 and Trial 2 from Dog 9. The green squares surround the proximal regions, while the red squares surround the distal regions. A–D, Activation maps for S_2–S_5 APs for Trial 1, in which an SLSI premature stimulus sequence was applied to the RV of Dog 4. This trial was in the "good" category of agreement scores with coupled maps model predictions of discordant alternans patterns. E–H, Activation maps for S_2–S_5 APs for Trial 2, in which a SLSI premature stimulus sequence was applied to the RV of Dog 9. This trial was in the "poor" category of agreement scores with coupled maps model predictions of discordant alternans patterns. Regions of conduction block, on the S_5 AP wave fronts, which are closest to the stimulating electrode are indicated with pink arrows in D and H. AP indicates action potential; RV, right ventricle.

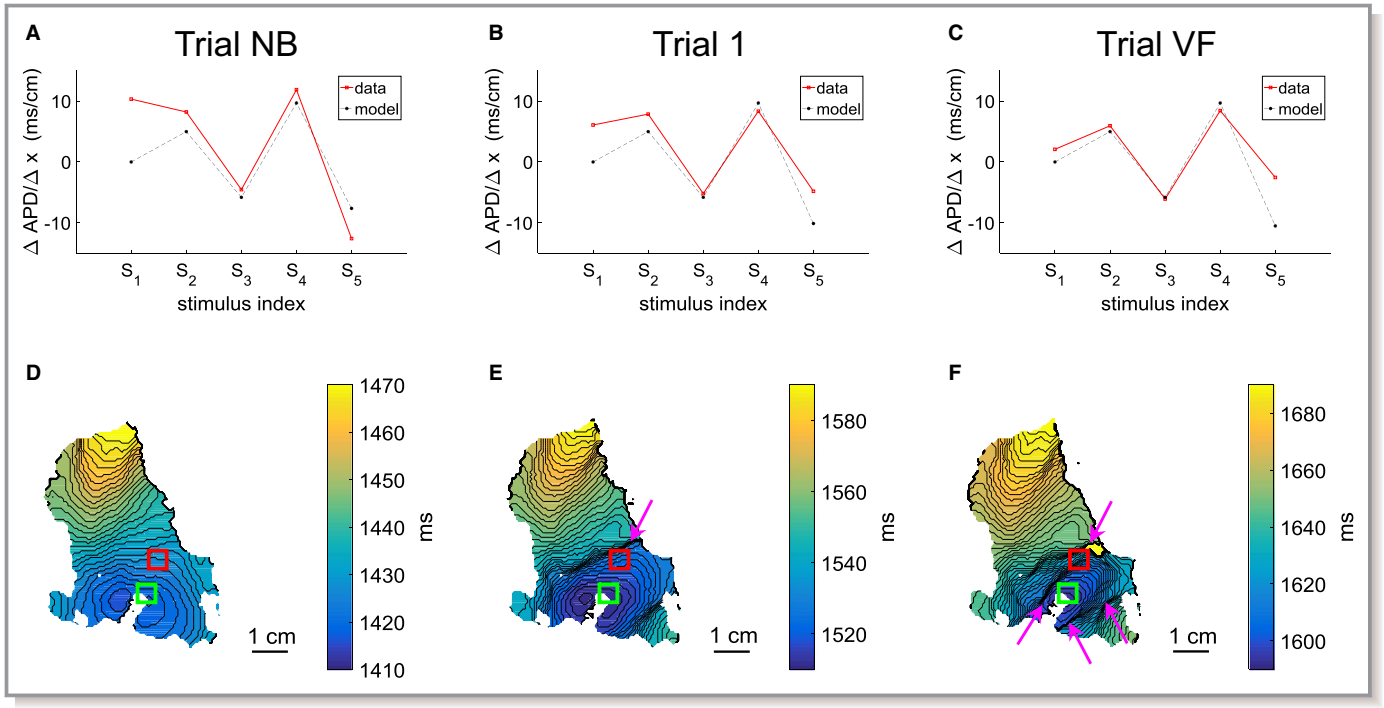

Figure 6. Spatial gradients of APD and activation maps for S_5 APs for Trials NB, 1, and VF. A–C, ΔAPD/Δx vs stimulus index for Trial NB (SLSL, left), Trial 1 (SLSI, middle) and Trial VF (SLSI, right), recorded from tests of premature stimulus sequences on RV of Dog 4. Black dashed lines with asterisks indicate model-predicted values, and red solid lines with squares represent the measured values. D–F, 2-dimensional spatial maps of activation times (in milliseconds) measured on the endocardial surface for the S_5 AP, for Trial NB (left), Trial 1 (middle), and Trial VF (right). The green square surrounds the proximal region, while the red square surrounds the distal region. Regions of conduction block, on the S_5 AP wave fronts, which are closest to the stimulating electrode, are indicated with pink arrows in E and F. AP indicates action potential; APD, action potential duration; NB, no block; RV, right ventricle; VF, ventricular fibrillation.

To test the VF-Prediction Hypothesis, our data set was the complete list of categories of premature stimulus sequences tested in vitro, along with the outcome (whether sustained VF was induced), as shown in Table S1. The sequences most commonly associated with sustained VF were SLSI, which preceded 40% of the recorded inductions, followed by SI, which preceded 27% of the inductions. Our premature stimulus protocol included successive tests of SLSL, SLSI, and SLSS, which were achieved through progressive reductions of S_4S_5, but SLSS sequences were often unreachable due to instances of VF induced by SLSI (S_4S_5 could not be reduced further without inducing an arrhythmia). These results are consistent with the predictions of the coupled maps model, which tended to classify SLSI and SLSS sequences as likely to induce VF. Model predictions and experimental outcomes corresponding to the n=184 sets of (sequence, VF outcome) pairs shown in Table S1 are summarized in Table 5. Using the model prediction as a binary predictor of the ability to induce sustained VF yielded a sensitivity of 53% and a specificity of 82%. Applying the Gelzer et al[27,28] statistical method to the data showed that the effect of the model prediction was significant (P<0.0001) according to an effect likelihood ratio test. The P value for the effect of dog (P=0.0485) was close to our chosen threshold for significance (P=0.05), and the implications of this result are explored in the Discussion section. The regression coefficient for the model prediction effect was 1.26 with a standard error of 0.32 (P<0.0001). Next, a Wald test applied to the GEE logistic regression model of VF outcomes, with clustering by dog, showed that the effect of the coupled maps model prediction was significant (P=0.0046), with a regression coefficient estimate of 1.63 and standard error 0.57. The scale parameter estimate was 1.0, with a standard error of 0.98.

To test the Reentry-Precedes-VF Hypothesis, we performed a qualitative visual review of the 15 movies (Movies S3 and S5–S18) where sustained VF was observed to follow sequences of premature stimuli. Fourteen (93%) of these instances of VF were judged as likely to have been induced by reentry, according to the approach described in the Methods section. For the remaining instance (Movie S5), VF appeared to have been preceded by spontaneous focal complexes, rather than reentrant waves. Figures 7 and 8 illustrate the types of visual assessments that were used to distinguish between focal complexes and reentrant waves.

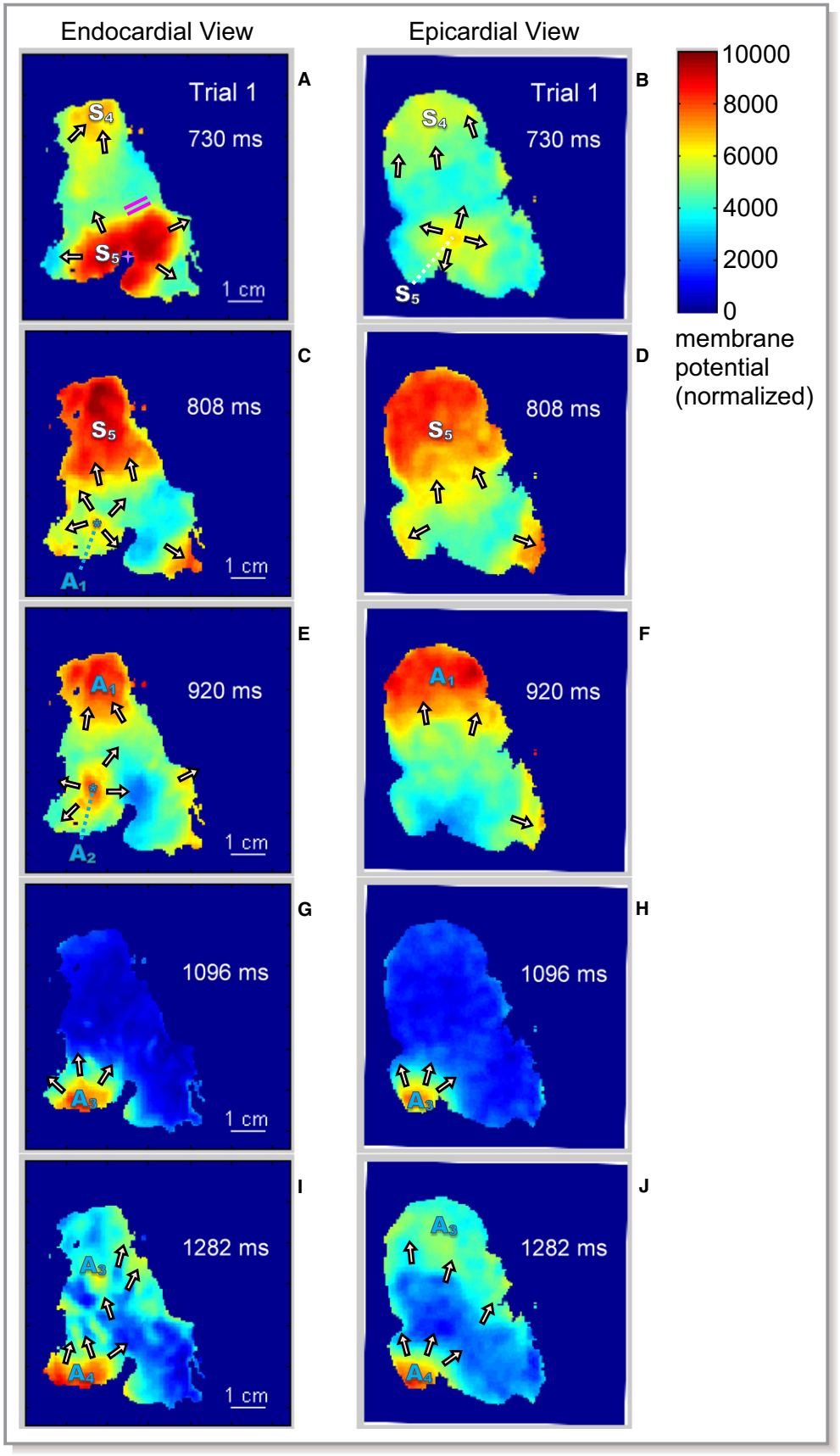
Endocardial View
Epicardial View
A
Trial 1
730 ms
S4
S5
1 cm
B
Trial 1
730 ms
S4
S5
C
808 ms
S5
A1
1 cm
D
808 ms
S5
E
920 ms
A1
A2
1 cm
F
920 ms
A1
G
1096 ms
A3
1 cm
H
1096 ms
A3
I
1282 ms
A3
A4
1 cm
J
1282 ms
A3
A4
10000
8000
6000
4000
2000
0
membrane potential (normalized)

Figure 7. Spontaneous complexes following S_5 AP during Trial 1. Endocardial view (left), with corresponding epicardial view (right) of 2-dimensional spatial membrane potential data (dimensionless, normalized to a scale of 0 to 10 000), recorded from a test of an SLSI premature stimulus sequence on RV of Dog 4. Sustained VF was not induced. The spatial scales are the same in both the endocardial and epicardial images, and the epicardial view was registered to match the orientation of the endocardial view. Arrows indicate the directions of propagation of AP wave fronts and wave backs. A, Frame recorded at 730 ms shows the emergence of the S_5 AP, along with the retreating wave back of the S_4 AP. The stimulating electrode tip is located near the purple star. Pink parallel lines indicate the location of conduction block. B, Epicardial view at 730 ms. The S_4 AP wave back was retreating, and the S_5 AP had reached the epicardial surface. C and D, Views of the exiting S_5 AP wave back at 808 ms. In C, a spontaneous complex, labeled A_1, appeared at the location marked with a blue asterisk. A_1 was classified as a "focal" spontaneous complex, since A_1 appeared to emerge spontaneously from a localized region on the endocardium, rather than being caused by reentry. E and F, Views of the exiting A_1 AP wave back at 920 ms. In E, another spontaneous focal complex, labeled A_2, emerged from the location marked with a blue asterisk. G and H, Views from 1096 ms, showing a spontaneous focal complex, labeled A_3, which appeared to emerge from the boundary of the RV (in the lower left corner of the image) and proceeded to propagate throughout the ventricle. I and J, Views from 1282 ms, showing a spontaneous focal complex, labeled A_4, which appeared to emerge from the same location as A_3. A_4 subsequently propagated throughout the ventricle. After the events shown in this figure, 4 additional spontaneous complexes that behaved similarly to A_3 and A_4 were observed after A_4, but no reentrant activity was observed. A movie of the optical mapping data from this trial is available in Movie S2. AP indicates action potential; RV, right ventricle; VF, ventricular fibrillation.

Discussion

New Findings and Comparisons With Other Studies

The present study expands upon the mechanistic insights of earlier work,[27,28] which examined the relationship between premature complexes and VF. As described by Gelzer et al[27] and outlined in Figure 1, it is hypothesized that specific sequences of premature stimulus intervals (including SLSS and similar sequences) can, through the influence of APD and CV restitution, cause enhanced spatial dispersion of repolarization, leading to spatially discordant APD alternans, conduction block, reentry, and VF. This sequence of events provides an explanation for the observation that certain patterns of premature complexes, including short-long-short,[5] long-short[3] and short-long,[4] promote reentry, VT, and VF. In this study, we confirmed that the coupled maps model, when supplied with APD restitution data from canine right ventricles, predicted the presence of discordant alternans, in the form of beat-to-beat patterns of sign changes in spatial gradients of APD and DI, when compared with observations from optical mapping data. Next, we showed that the model predicted which sequences of premature stimuli were more likely to induce conduction block in vitro. The logistic regression analyses showed that the model-based classification scheme (≥25% of stimulus combinations yielding block) was a statistically significant predictor of VF in vitro. Our visual assessment of optical recordings indicated that instances of sustained VF were typically preceded by reentry.

Discordant alternans

The results of the posterior probability analysis were consistent with our Alternans-Pattern-Prediction Hypothesis, which claims that the computational model will correctly predict in vitro patterns in spatial gradients of APD and DI resulting from the premature complexes. However, observed gradients did not always match model-predicted patterns, as shown in Figure 4C and 4D and Table 2. This large variability in observed patterns may have been due to variations in the measured APD and DI gradients across individuals, uncertainties in these measurements, and factors (such as spatial heterogeneity of APD and DI) that influence the measured values but are not present in the coupled maps model.

The largest measured spatial gradient in APD shown in Figure 4A has a magnitude of approximately 8 ms/cm and corresponds to a trial where the S_5 wave front encountered block in vitro. This magnitude lies within the range of block-inducing APD gradients (5–50 ms/cm) found in the simulation study of Sampson and Henriquez,[38] but well below the range of 100 to 1200 ms/cm reported by Restivo et al for live infarcted canine hearts.[39] A number of factors may account for disagreement between our gradient values and those of certain other studies, including differences in experimental conditions, stimulus protocols, and measurement methods.

Regarding the effects of noise, Uzelac and Fenton observed that, for an optical mapping setup that is very similar to ours in terms of equipment, frame rates, and experimental procedures, the signal-to-noise ratio is rarely >10 for membrane potential fluorescence data.[40] To help address uncertainties in the optical signals, in our Bayesian

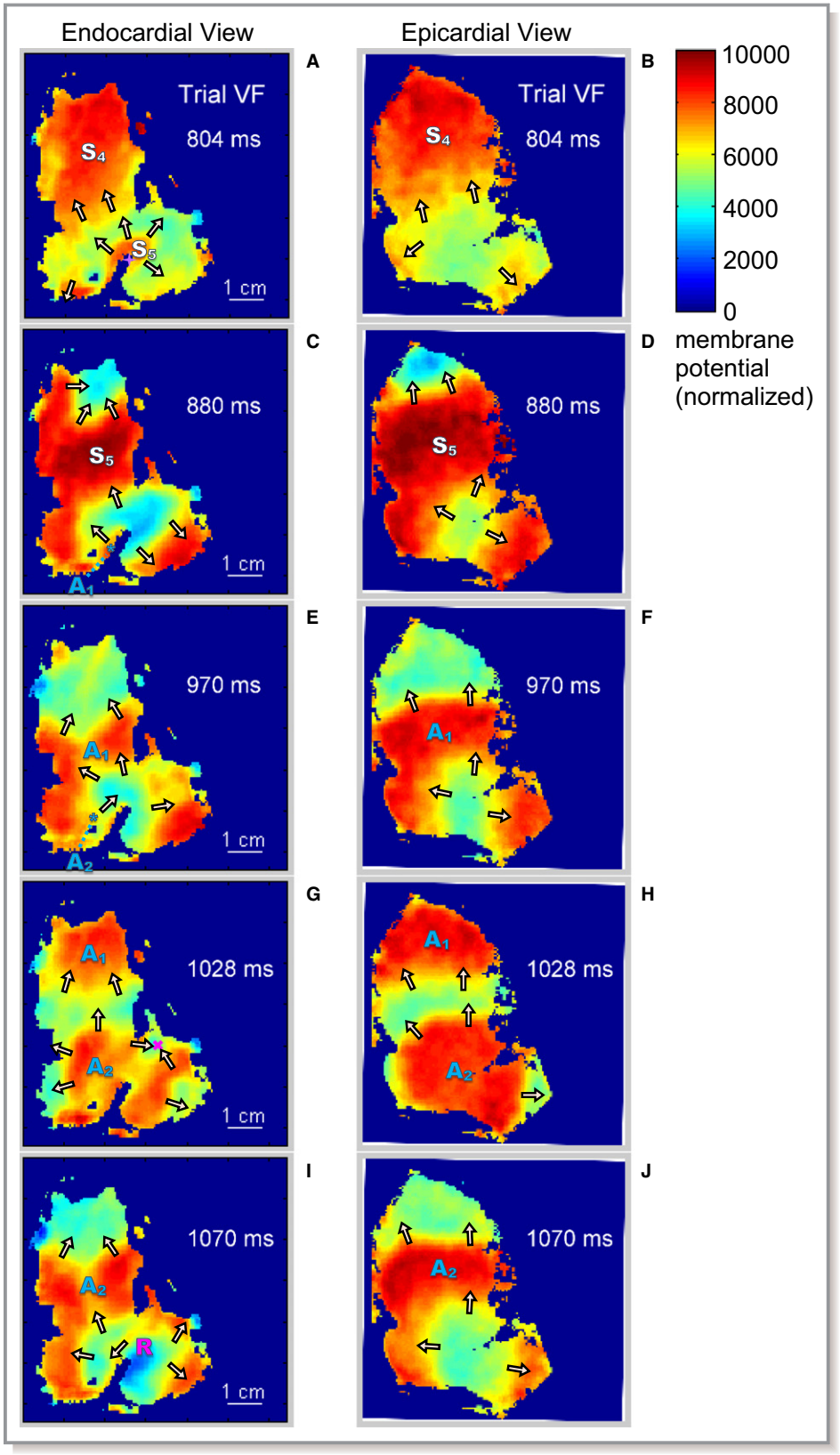
Endocardial View
Epicardial View
A
B
C
D
E
F
G
H
I
J
Trial VF
804 ms
880 ms
970 ms
1028 ms
1070 ms
S4
S5
A1
A2
R
1 cm
10000
8000
6000
4000
2000
0
membrane potential (normalized)

Figure 8. Reentry following S_5 AP during Trial VF. Endocardial view (left), with corresponding epicardial view (right) of 2-dimensional spatial membrane potential data (dimensionless, normalized to a scale of 0 to 10 000), recorded from a test of an SLSI premature stimulus sequence on RV of Dog 4. Sustained VF was induced. The spatial scales are the same in both the endocardial and epicardial images, and the epicardial view was registered to match the orientation of the endocardial view. Arrows indicate the directions of propagation of AP wave fronts and wave backs. A, Frame recorded at 804 ms shows the emergence of the S_5 AP, along with the retreating wave back of the S_4 AP. The stimulating electrode tip is located near the purple star. B, Epicardial view at 804 ms. The S_4 AP wave back was retreating, while the S_5 AP had not yet reached the epicardial surface. C and D, Views of S_5 AP propagation at 880 ms. In C, a spontaneous complex, labeled A_1, appeared at the location marked with a blue asterisk. E and F, Views of A_1 AP propagation at 970 ms. In E, a spontaneous complex, labeled A_2, emerged from the A_1 AP, at the location marked with a blue asterisk, and propagated into the region near the electrode. G and H, Views from 1028 ms, showing the propagation of the A_2 AP. In G, a portion of the A_2 wave front encountered slow conduction near the region marked with a pink "x." I and J, Views from 1070 ms, showing the propagation of the A_2 AP. After activating the region of slow conduction, a portion of the A_2 AP reentered the region near the electrode, as shown in I, where the reentrant wave front is labeled with an "R." After the events shown in this figure, another cycle of reentry, similar to the process shown in G and I, was observed, followed by increasingly disorganized propagation and VF. A movie of the optical mapping data from this trial is available in Movie S3. AP indicates action potential; RV, right ventricle; VF, ventricular fibrillation.

analysis of discordant alternans, we referred to a base case of 12.5% (=1/8), which is the prior probability for all 8 possible sequences of sign patterns, if no data were available and no pattern of signs were present. That is, we can consider a worst-case scenario where our $\Delta(\Delta APD/\Delta x)$ (or $\Delta(\Delta DI/\Delta x)$) data are essentially all noise, in which case we could liken the process to a random sign generator that produces 1 of 2 values, "+" or "−," for each of the S_2S_3, S_3S_4, and S_4S_5 intervals. If the random binary sign generator behaves as a sequence of unweighted, independent coin tosses, then the probability of any ordered triple of 3 coin tosses following the (−, +, −) pattern, or any other pattern, is 12.5% because there are 2^3=8 possible sequences of 3 signs. Because the posterior probabilities for the (−, +, −) discordant alternans pattern were much larger than 12.5%, this is an indication that a mechanism promoting the discordant pattern is likely present in the data. The signless case, where the beat-to-beat change in either spatial gradient is zero, could also have been considered, but zero values did not appear in our $\Delta(\Delta APD/\Delta x)$ or $\Delta(\Delta DI/\Delta x)$ data.

Conduction block

The 0% false-positive rate indicates that the model is accurate when it predicts that block will occur, which was consistent with our Block-Prediction Hypothesis. However, examination of the data revealed that the model predicted fewer instances of block than were actually observed. A probable reason for the underprediction of in vitro block is the spatially homogeneous nature of the model parameters. Presumably, including heterogeneities in the model would increase the frequency of block occurrences in silico.

In Gelzer et al,[27,28] a fixed fiber length of 7 cm was used for all coupled maps simulations, and no attempt was made in those studies to calibrate the simulated fiber lengths to match

Table 4. Percentages of S_5 APs, Organized by Experimental Observation of Conduction Block vs Model Prediction of Conduction Block

	Model Prediction	
Experimental Outcome	Block Occurred, %	Block Did Not Occur, %
Block was observed	100 (9/9)	56 (5/9)
Block was not observed	0 (0/9)	44 (4/9)

APs indicates action potentials.
"Experimental Outcome" refers to whether block of the S_5 AP wave front was observed in vitro, and "Model Prediction" refers to whether block occurred on the S_5 AP wave front in corresponding simulations of the coupled maps model. Numbers in parentheses are the percentages rewritten as fractions of the total number of S_5 APs in each of the 2 model prediction categories.

Table 5. Percentages of Stimulus Sequence Categories, Organized by Experimental Outcome vs Model Prediction

	Model Prediction	
Experimental Outcome	≥25% of Combinations Yielded Block, %	<25% of Combinations Yielded Block, %
VF was inducible	21 (8/39)	5 (7/145)
VF could not be induced	79 (31/39)	95 (138/145)

VF indicates ventricular fibrillation.
"Experimental Outcome" refers to whether sustained VF was induced in vitro, and "Model Prediction" refers to whether ≥25% or <25% of the combinations in the stimulus sequence category yielded block in simulations of the coupled maps model. Numbers in parentheses are percentages rewritten as fractions of the total number of stimulus sequence categories tested in each of the 2 model prediction categories.

closely with the sizes of the intact hearts. In this study, we used the same fiber length of 7 cm for all simulations, even though the RVs varied in size (4–8 cm in length, 4–5 cm in width). The fact that the coupled maps model was found to underpredict block in vitro suggests that reducing certain simulated fiber lengths, to match more closely with the smaller RVs, would not improve the accuracy of the block predictions. Reducing the length of the fiber makes block even less likely to occur in silico, since there is less room for a simulated AP wave front to catch up with a slow-moving wave back. Including spatial heterogeneity in the model may be a more promising means of increasing the predicted block rate, compared with reducing the fiber length.

As described in the Methods section, we used a 2-part definition of conduction block, where (1) CV magnitude between 0.5 cm/s and 10 cm/s and (2) visual evidence that the wave front was changing direction across the proposed line of block were both required to conclude that conduction block had occurred in vitro. During the study design phase, we included part 2 of the definition because we anticipated a need to distinguish between instances of "plane-wave" slowing, where a wave front slows temporarily, but then proceeds along its initial heading, compared with instances where a wave front was slowing and changing its direction. In retrospect, the second part of the definition did not need to be included because all of the observed instances of in vitro block on the S_5 AP wave fronts satisfied both parts 1 and 2 of the definition. Hence, if the definition of conduction block were reduced to just the first portion (0.5 cm/s $<$CV magnitude $\leq$10 cm/s), the block comparison results in Table 4 would be unchanged. This simpler definition of block would enhance the reproducibility of the methods.

By providing a direct comparison with in vitro block instances, our findings constitute an extension of the work of Gelzer et al,[27,28] where limitations of the in vivo experimental setup prevented direct observation of block. Other studies[24,41] have made comparisons between numerical predictions and in vitro measurements of block but differed from our approach in one or more respects. For example, Fox et al[24] examined discordant alternans and block, using a coupled maps model, an ionic model, and data from Purkinje fibers in vitro. Their study provided evidence for a mechanism similar to the one described in Figure 1, but their approach was centered on rapid pacing rather than premature, irregularly timed stimuli.

Reentry and sustained VF

We found that the coupled maps model's classification of whether a sequence was likely to cause block was a statistically significant predictor of sustained VF. These results corroborate those of Gelzer et al,[27,28] where the same type of prediction method was found to be a statistically significant predictor of VF in canines in vivo. SLSI was the sequence that most often preceded VF in vitro, accounting for 40% of recorded inductions. In our protocol, tests of SLSI progressed to SLSS through successive reductions of S_4S_5. This process was often interrupted by VF induction following an SLSI sequence, whereas SLSS was reached more frequently in vivo.[27] Despite this difference, the results are consistent with predictions of the coupled maps model, which tended to classify both SLSI and SLSS as arrhythmogenic.

Our application of the statistical approach of Gelzer et al,[27,28] showed that the effect of dog in the logistic regression model was close to the threshold for statistical significance. This result is not consistent with those of the earlier studies,[27,28] where the effect of dog was found to be insignificant. From the perspective of a computational modeler, it is more convenient to have an insignificant effect of dog because a lack of significance suggests that the coupled maps parameters may not need to be fine-tuned to each individual in order to generate accurate VF predictions. Hence, referring to the in vitro effect of dog as significant is the less favorable (or more conservative) interpretation of our result. Table S4 summarizes how the statistical results were affected by uncertainties in ERP measurements.

Table 5 indicates a false-positive rate of 18% for VF predictions, which is higher than the 2% reported in Gelzer et al.[27] The positive predictive values for the in vitro and in vivo[27] studies were 21% and 75%, respectively, while corresponding negative predictive values were 95% and 92%. While the model accurately identified premature stimulus sequences that did not induce VF both in vivo and in vitro, the low in vitro positive predictive value was not consistent with the VF-Prediction Hypothesis, in the sense that the model performed relatively poorly at identifying VF-inducing sequences. A likely explanation is that the in vitro RV preparations, due to being smaller than intact hearts, may have been less intrinsically heterogeneous than the intact hearts studied by Gelzer et al[27]; thus, the risk of sustained VF was greater in vivo. In addition, the in vitro preparations may have had insufficient myocardial mass to provide a VF risk that was comparable with that of intact hearts. Determining the causes of the discrepancies between the in vitro and in vivo outcomes is a subject of ongoing work.

Our conclusion that 93% of the observed instances of sustained VF were preceded by reentry, which was largely consistent with our Reentry-Precedes-VF Hypothesis, was based on a qualitative visual review of the optical recordings. Examples of our review process are given in Figures 7 and 8. Movies of the sustained VF inductions have been included in the Supplement so that readers may make their own assessments.

Hypothesized mechanism for VF

A main focus of this study was to determine whether the observations agreed with the block and VF mechanisms described in Figure 1. Detailed comparisons between the hypothesized mechanism and events observed in selected trials are provided in Figures 4 through 8 and in Table 3. To give an idea of the types of correspondences and discrepancies we witnessed, we refer to the trials first shown in Figure 4, which were chosen as examples of good (Trial 1) and poor (Trial 2) agreement between predicted and measured gradients. Examination of the optical data, as shown in Figure 5, revealed that the S_5 wave front encountered conduction block in both trials, but sustained VF was not observed in either trial. The lack of VF in Trial 1 appeared to depend on the length of S_4S_5, as reducing S_4S_5 in a series of trials following Trial 1 produced block followed by reentry of the S_5 AP and, subsequently, sustained VF (see Figures 6 through 8 in the Results section and Movies S2 and S3). By contrast, reducing S_4S_5 in trials subsequent to Trial 2 sometimes yielded spontaneous complexes or nonsustained VF (data not shown), but sustained VF was not induced.

To determine possible causes for the poor agreement between observed Trial 2 gradients and model predictions of $\Delta APD/\Delta x$ and $\Delta DI/\Delta x$ sign patterns, we note two ways in which Trial 2 differed from Trial 1, namely, that (1) Trial 2 showed more complex AP propagation patterns, including a larger number of regions of conduction block, including block on the S_1 wave front (Figure 2), and (2) Trial 2 had a shorter distance between proximal and distal regions. The distances between proximal and distal regions, measured from the outer vertices of the proximal and distal squares, ranged from 1.1 to 1.6 cm over the 9 dogs. Comparing model agreement scores in Table 2 to these distances has not revealed any clear relationship between scores and distances. However, data from Dog 9 (the source of Trial 2) accounted for 3 out of a total of 5 trials that collectively appeared in either the APD- or DI-based "poor" categories in Table 2. Hence, it is possible that there were differences specific to either Dog 9's right ventricle, which could also explain its more complex S_1 AP propagation shown in Figure 2I, or the region chosen for APD and DI gradient measurements for that ventricle, that accounted the poor agreement with model-predicted sign patterns.

The varying patterns of agreement and disagreement with model predictions were not unexpected. Our coupled maps model makes predictions about conduction block, but on its own does not predict when block will subsequently degenerate into reentry. Nevertheless, block of action potential waves is widely thought to render the resulting wave pattern more susceptible to reentry, which, under the right conditions, leads to the development of VT, wave break, and/or VF. Thus, it is not surprising that we see a tendency, but not an outright inevitability, for conditions theoretically predicted to result in block to also lead to these other, more serious wave patterns.

Study Limitations

While the 1D coupled maps model is computationally efficient, it can represent only part of one possible pathway to VF and does not make any predictions about higher-dimensional reentrant phenomena. Modeling these phenomena or generating predictions for multiple distinct VF mechanisms would require us to use more complex computational models. Other links in the VF mechanism (eg, a possible relationship between block and reentry) could have been explored here, but to maintain tractability, the study was limited to the relationships covered by our hypotheses.

A limitation of our experimental setup is that it only allows measurements to be taken from the endocardial and epicardial surfaces, which is insufficient to capture all 3 spatial components of CV. In this study, measured CV magnitudes were used to distinguish between fast and slow propagation along the endocardial surfaces, and conduction block on a surface was defined on the basis of the measurable components of CV. However, block confined to the ventricle interior is not detectable using this setup. Determining the impact of the missing CV component on the accuracy of conduction block measurements and CV restitution parameters is a subject intended for future work.

Following the methodology of Gelzer et al,[27,28] we estimated one set of APD restitution parameters per dog, using pace-down data from each dog, while CV parameters were fit to microelectrode data from a different study[32] and were held fixed across dogs, except for the DI_{min} parameter, which affected CV predictions and was obtained from the data from each dog. An alternative approach would be to recalibrate the remaining CV parameters using measurements from the optical data, to determine whether recalibrating the parameters would improve the accuracy of our predictions.

In addition to the CV parameters, other model parameters and settings (such as fiber length) could be adjusted to determine their effect on the quality of the predictions. However, to facilitate comparisons, one of our main goals in this study was to keep the model calibration procedures as consistent as possible with those of Gelzer et al,[27,28] rather than to determine which adjustments to the model would maximize the accuracy of its predictions. We feel that the latter goal is sufficiently complex to warrant a separate study.

Certain portions of the data analysis relied on qualitative visual assessments. To check the second part of the conduction block definition, we viewed the activation maps to determine whether wave fronts had changed direction across the proposed line of block. As discussed earlier, the second part of the definition, along with the corresponding visual review, could have been eliminated without having any impact on the results. In addition, determining whether reentry preceded VF involved reviewing movies of AP propagation to distinguish reentrant behavior from other causes. Ideally, this portion of the analysis could be automated, but this would require us to find and adapt an appropriate identification algorithm or to develop a new approach, either of which seems sufficiently challenging to be better suited for a separate study. In lieu of an automated method, we have provided examples of nonreentrant behavior (in the form of spontaneous focal complexes) and reentrant waves in Figures 7 and 8 to illustrate our classification approach.

Conclusions

In this study, we investigated a theoretical mechanism linking premature complexes to VF. To accomplish this, we collected optical mapping data from canine right ventricles, and compared in vitro observations with predictions from a 1D coupled maps model. The model was shown to be effective in predicting (1) patterns of discordant alternans, (2) which premature stimulus sequences were more likely to induce conduction block, and (3) which premature stimulus sequences were unlikely to induce VF. The confirmation of the model's ability to predict alternans and block, along with the confirmation that reentry typically preceded VF, provided evidence for the theoretical mechanism beyond what was possible using the methods of Gelzer et al.[27,28] We continue to find that, while our 1D model clearly does not include all the dynamics present, it is nevertheless remarkable in its ability to predict and reasonably represent the dynamics of block leading up to VT and VF onset, despite its simplicity. Thus, our study suggests that the discordant-alternans mechanism observed in the model is likely to be playing an important role in the development of instances of VT and VF that follow premature beats. This line of research may eventually lead to improved block and VF forecasting algorithms, along with programs that evaluate the arrhythmogenic potential of planned patterns of premature stimuli, which could lead to safer antitachycardia pacing strategies for implantable devices.

Acknowledgments

The authors thank Trine Krogh-Madsen, whose questions aided us in improving the Discussion section. We acknowledge Min Chul Shin for aiding in development of movie generation scripts, and Hyundo Reiner for helping to validate filtering methods used in the Java-based data processing software. We also thank Fathima Zahra Kamil Faiz for assistance with refining experimental methods, Mohammed Premjee and Jeffrey Fitch for their help with recording certain experimental settings, and Francis Lee and Andrea Liu for contributing to the data processing. We would also like to thank the working group on Prediction and Control of Cardiac Alternans at the National Institute for Mathematical and Biological Synthesis (http://www.nimbios.org/workinggroups/WG_arrhythmias) for useful discussions. In addition, we are grateful to our anonymous reviewers, whose suggestions helped us to improve the clarity of the manuscript.

Sources of Funding

This study was supported by Award Number R01HL089271 from the National Heart, Lung, and Blood Institute. The content is solely the responsibility of the authors and does not necessarily represent the official views of the National Heart, Lung, and Blood Institute or the National Institutes of Health. In addition, this material is based upon work supported by the National Science Foundation under Grant No. 1446675.

Disclosures

None.

References

1. Kong MH, Fonarow GC, Peterson ED, Curtis AB, Hernandez AF, Sanders GD, Thomas KL, Hayes DL, Al-Khatib SM. Systematic review of the incidence of sudden cardiac death in the United States. *J Am Coll Cardiol*. 2011;57:794–801.
2. Teodorescu C, Reinier K, Dervan C, Uy-Evanado A, Samara M, Mariani R, Gunson K, Jui J, Chugh SS. Factors associated with pulseless electric activity versus ventricular fibrillation: the Oregon sudden unexpected death study. *Circulation*. 2010;122:2116–2122.
3. Kay GN, Plumb VJ, Arciniegas JG, Henthorn RW, Waldo AL. Torsade de pointes: the long-short initiating sequence and other clinical features: observations in 32 patients. *J Am Coll Cardiol*. 1983;2:806–817.
4. Gomes JA, Alexopoulos D, Winters SL, Deshmukh P, Fuster V, Suh K. The role of silent ischemia, the arrhythmic substrate and the short-long sequence in the genesis of sudden cardiac death. *J Am Coll Cardiol*. 1989;14:1618–1625.
5. el-Sherif N, Gough WB, Restivo M. Reentrant ventricular arrhythmias in the late myocardial infarction period: mechanism by which a short-long-short cardiac sequence facilitates the induction of reentry. *Circulation*. 1991;83:268–278.
6. Koller BS, Karasik PE, Solomon AJ, Franz MR. Relation between repolarization and refractoriness during programmed electrical stimulation in the human right ventricle: implications for ventricular tachycardia induction. *Circulation*. 1995;91:2378–2384.
7. Avitall B, McKinnie J, Jazayeri M, Akhtar M, Anderson AJ, Tchou P. Induction of ventricular fibrillation versus monomorphic ventricular tachycardia during programmed stimulation. Role of premature beat conduction delay. *Circulation*. 1992;85:1271–1278.
8. Karma A. Electrical alternans and spiral wave breakup in cardiac tissue. *Chaos*. 1994;4:461–479.
9. Cao J-M, Qu Z, Kim Y-H, Wu T-J, Garfinkel A, Weiss JN, Karagueuzian HS, Chen P-S. Spatiotemporal heterogeneity in the induction of ventricular fibrillation by rapid pacing: importance of cardiac restitution properties. *Circ Res*. 1999;84:1318–1331.
10. Qu Z, Weiss JN, Garfinkel A. Cardiac electrical restitution properties and stability of reentrant spiral waves: a simulation study. *Am J Physiol Heart Circ Physiol*. 1999;276:H269–H283.

11. Pak H-N, Hong SJ, Hwang GS, Lee HS, Park S-W, Ahn JC, Moo Ro Y, Kim Y-H. Spatial dispersion of action potential duration restitution kinetics is associated with induction of ventricular tachycardia/fibrillation in humans. *J Cardiovasc Electrophysiol*. 2004;15:1357–1363.
12. Weiss JN, Qu Z, Chen P-S, Lin S-F, Karagueuzian HS, Hayashi H, Garfinkel A, Karma A. The dynamics of cardiac fibrillation. *Circulation*. 2005;112:1232–1240.
13. Cherry EM, Fenton FH, Gilmour RF Jr. Mechanisms of ventricular arrhythmias: a dynamical systems-based perspective. *Am J Physiol Heart Circ Physiol*. 2012;302:H2451–H2463.
14. Fox JJ, Riccio ML, Drury P, Werthman A, Gilmour RF Jr. Dynamic mechanism for conduction block in heart tissue. *New J Phys*. 2003;5:101.
15. Comtois P, Vinet A, Nattel S. Wave block formation in homogeneous excitable media following premature excitations: dependence on restitution relations. *Phys Rev E*. 2005;72:031919.
16. Qu Z, Garfinkel A, Weiss JN. Vulnerable window for conduction block in a one-dimensional cable of cardiac cells, 1: single extrasystoles. *Biophys J*. 2006;91:793–804.
17. Qu Z, Garfinkel A, Weiss JN. Vulnerable window for conduction block in a one-dimensional cable of cardiac cells, 2: multiple extrasystoles. *Biophys J*. 2006;91:805–815.
18. Otani NF. Theory of action potential wave block at-a-distance in the heart. *Phys Rev E*. 2007;75:021910.
19. Tran DX, Yang M-J, Weiss JN, Garfinkel A, Qu Z. Vulnerability to re-entry in simulated two-dimensional cardiac tissue: effects of electrical restitution and stimulation sequence. *Chaos*. 2007;17:043115.
20. Zheng Y, Wei D, Fang Z, Zhu X. Influences of sites and protocols on inducing ventricular fibrillation: a computer simulation study. *Conf Proc IEEE Eng Med Biol Soc*. 2010;2010:2005–2008.
21. Courtemanche M, Glass L, Keener JP. Instabilities of a propagating pulse in a ring of excitable media. *Phys Rev Lett*. 1993;70:2182–2185.
22. Watanabe MA, Fenton FH, Evans SJ, Hastings HM, Karma A. Mechanisms for discordant alternans. *J Cardiovasc Electrophysiol*. 2001;12:196–206.
23. Vinet A. Quasiperiodic circus movement in a loop model of cardiac tissue: multistability and low dimensional equivalence. *Ann Biomed Eng*. 2000;28:704–720.
24. Fox JJ, Riccio ML, Hua F, Bodenschatz E, Gilmour RF Jr. Spatiotemporal transition to conduction block in canine ventricle. *Circ Res*. 2002;90:289–296.
25. Fox JJ, Gilmour RF Jr, Bodenschatz E. Conduction block in one-dimensional heart fibers. *Phys Rev Lett*. 2002;89:198101.
26. Otani NF. Termination of reentrant cardiac action potential propagation using far-field electrical pacing. *IEEE Trans Biomed Eng*. 2011;58:2013–2022.
27. Gelzer ARM, Koller ML, Otani NF, Fox JJ, Enyeart MW, Hooker GJ, Riccio ML, Bartoli CR, Gilmour RF Jr. Dynamic mechanism for initiation of ventricular fibrillation in vivo. *Circulation*. 2008;118:1123–1129.
28. Gelzer ARM, Otani NF, Koller ML, Enyeart MW, Moise NS, Gilmour RF Jr. Dynamically-induced spatial dispersion of repolarization and the development of VF in an animal model of sudden death. *Comput Cardiol*. 2009;36:309–312.
29. Koller ML, Riccio ML, Gilmour RF Jr. Dynamic restitution of action potential duration during electrical alternans and ventricular fibrillation. *Am J Physiol Heart Circ Physiol*. 1998;275:H1635–H1642.
30. Gizzi A, Cherry E, Gilmour RF Jr, Luther S, Filippi S, Fenton FH. Effects of pacing site and stimulation history on alternans dynamics and the development of complex spatiotemporal patterns in cardiac tissue. *Front Physiol*. 2013;4:71.
31. Watanabe M, Otani NF, Gilmour RF Jr. Biphasic restitution of action potential duration and complex dynamics in ventricular myocardium. *Circ Res*. 1995;76:915–921.
32. Riccio ML, Hua F, Lomonte DJ, Venator KR, Cerda-Gonzalez S, Gilmour RF Jr. Effects of hypocalcemia on electrical restitution and ventricular fibrillation. *Conf Proc IEEE Eng Med Biol Soc*. 2009;2009:4182–4185.
33. DeGroot MH. *Optimal Statistical Decisions*. New York: McGraw-Hill; 1970.
34. Bernardo JM. Reference analysis. In: Dey KD, Rao CR, eds. *Handbook of Statistics 25: Bayesian Thinking: Modeling and Computation*. Amsterdam: Elsevier B. V.; 2005:17–90.
35. Choirat C, Honaker J, Imai K, King G, Lau O. Zelig: Everyone's Statistical Software. Version 5.1.6; 2018. Available at: http://zeligproject.org/. Accessed May 17, 2018.
36. Imai K, King G, Lau O. Toward a common framework for statistical analysis and development. *J Comput Graph Stat*. 2008;17:892–913.
37. Lam P. Logit-Gee: General Estimating Equation for Logistic Regression. In Choirat C, Gandrud C, Honaker J, Imai K, King G, Lau O, *Zelig: Everyone's Statistical Software*. 2011. Available at: http://zeligproject.org/. Accessed May 17, 2018.
38. Sampson K, Henriquez C. Simulation and prediction of functional block in the presence of structural and ionic heterogeneity. *Am J Physiol Heart Circ Physiol*. 2001;281:H2597–H2603.
39. Restivo M, Gough WB, el-Sherif N. Ventricular arrhythmias in the subacute myocardial infarction period. High-resolution activation and refractory patterns of reentrant rhythms. *Circ Res*. 1990;66:1310–1327.
40. Uzelac I, Fenton FH. Robust framework for quantitative analysis of optical mapping signals without filtering. *Comput Cardiol*. 2015;42:461–464.
41. Cabo C, Pertsov AM, Baxter WT, Davidenko JM, Gray RA, Jalife J. Wave-front curvature as a cause of slow conduction and block in isolated cardiac muscle. *Circ Res*. 1994;75:1014–1028.

SUPPLEMENTAL MATERIAL

Data S1. Stimulus Sequence Categories Tested In Vitro

As described in the main text, the first pacing protocol was used to test whether different combinations of premature stimuli would induce sustained VF. The complete list of sequences of premature stimuli that were tested, along with VF outcomes (whether sustained VF was induced), is given in Table S1. To aid in comparisons across dogs, the rows of the table are matched by sequence type, where possible, but this type of organization does not always reflect the exact order in which the sequences were tested.

The sequences most commonly associated with sustained VF were SLSI, which preceded 40% of the recorded inductions, followed by SI, which preceded 27% of the inductions. Our premature stimulus protocol included successive tests of SLSL, SLSI, and SLSS, which were achieved through progressive reductions of S_4S_5 (for more detail, see the Pacing Protocols section in the main text), but SLSS sequences were often unreachable due to instances of VF induced by SLSI (S_4S_5 could not be reduced further without inducing an arrhythmia). These results are consistent with the predictions of the coupled maps model, which tended to classify SLSI and SLSS sequences as likely to induce VF.

Table S1. Premature Stimulus Sequence Categories Tested In Vitro, with VF Outcomes

Dog 1		Dog 2		Dog 3		Dog 4		Dog 5		Dog 6		Dog 7		Dog 8		Dog 9	
Seq.	VF	Seq.	VF	Seq.	VF	Seq.	VF	Seq.	VF	Seq.	VF	Seq.	VF	Seq.	VF	Seq.	VF
L	no	L	no	L	no	L	no	L	no	L	no	L	no	L	no	L	no
I	no	I	no	I	no	I	no	I	no	I	no	I	no	I	no	I	no
S	yes	S	no	S	no	S	no	S	no	S	no	S	no	S	no	S	no
SL	no	SL	no	SL	no	SL	no	SL	no	SL	no	SL	no	SL	no	SL	no
SI	no	SI	yes	SI	no	SI	yes	SI	no	SI	no	SI	no	SI	yes	SI	yes
SS	no	SS	no	SS	yes			SS	no	SS	yes	SS	no				
SLL	no	SLL	no	SLL	no	SLL	no			SLL	no	SLL	no	SLL	no	SLL	no
SLI	no	SLI	no	SLI	no	SLI	no			SLI	no	SLI	no	SLI	no	SLI	no
SLS	no	SLS	no	SLS	no	SLS	no			SLS	no	SLS	no	SLS	no	SLS	no
SLSL	no	SLSL	no	SLSL	no	SLSL	no			SLSL	no	SLSL	no	SLSL	no	SLSL	no
SLSI	no	SLSI	yes	SLSI	yes	SLSI	yes			SLSI	yes	SLSI	no	SLSI	yes	SLSI	yes
SLSS	no											SLSS	no			SLSS	no
		SLLL	no	SLLL	no	SLLL	no			SLLL	no					SLLL	no
		SLLI	no	SLLI	no	SLLI	no			SLLI	no					SLLI	no
				SLLS	no	SLLS	no			SLLS	no					SLLS	no
SLII	no											SLII	no				
		SSL	no									SSL	no				
		SSI	no									SSI	no				
		LL	no	LL	no	LL	no			LL	no						
		LI	no	LI	no	LI	no			LI	no						
		LS	no	LS	no	LS	no			LS	no						
		LLL	no	LLL	no	LLL	no			LLL	no						
		LLI	no	LLI	no	LLI	no			LLI	no						
		LLS	no	LLS	no	LLS	no			LLS	no						
		LSL	no	LSL	no	LSL	no			LSL	no						
		LSI	no	LSI	no	LSI	yes			LSI	no						
		LSS	no	LSS	no	LSS	no			LSS	no						
		LII	no							LII	no						
		LIS	no							LIS	no						
				LLSL	no	LLSL	no										
				LLSI	no	LLSI	no										
				LLSS	no	LLSS	no										
				LLII	no	LLII	no										
SLIS	no	II	no	LSSL	no	LLIS	yes	SIL	no			SSS	no				
		IIL	no	LSSI	no	LLLL	no	SII	no								
		III	no	LSSS	no	LLLI	no	SIS	no								
		IIS	no			LLLS	no	SISL	no								
		IISL	no					SISI	no								
								SISS	no								
								SIII	no								
								SIIS	no								

Alternations in the Signs of Gradients in Successive APDs and DIs:

In the study of Δ(ΔAPD/Δx), a Bayesian statistical analysis was used, as described in the main text. Table S2 gives the resulting posterior probabilities that the components of the mean $\boldsymbol{\mu}$ have any given sequence of signs:

Table S2. Posterior Probabilities for Sequences of Signs of Mean Values of Δ(ΔAPD/Δx)

Sequence of signs of $\boldsymbol{\mu} = (\mu_1, \mu_2, \mu_3)^{\boldsymbol{T}}$	Probability
$(-,-,-)$	0.32%
$(-,-,+)$	0.04%
$(-,+,-)$	91.14%
$(-,+,+)$	0.18%
$(+,-,-)$	2.43%
$(+,-,+)$	0.33%
$(+,+,-)$	5.51%
$(+,+,+)$	0.06%

An analogous calculation was performed for Δ(ΔDI/Δx), leading to the following posterior probabilities in Table S3:

Table S3. Posterior Probabilities for Sequences of Signs of Mean Values of Δ(ΔDI/Δx)

Sequence of signs of $\boldsymbol{\mu} = (\mu_1, \mu_2, \mu_3)^{\boldsymbol{T}}$	Probability
$(-,-,-)$	0.01%
$(-,-,+)$	0.30%
$(-,+,-)$	82.14%
$(-,+,+)$	17.30%
$(+,-,-)$	0.01%
$(+,-,+)$	0.01%
$(+,+,-)$	0.23%
$(+,+,+)$	0.01%

We observe that, for both Δ(ΔAPD/Δx) and Δ(ΔDI/Δx), the $(-,+,-)$ sequence of signs is by far the most probable. This suggests that the underlying process tends towards producing the zig-zag pattern shown in Figure 4A in the main text.

The $(-,+,-)$ pattern of signs has the highest posterior probability in both cases, which agrees with the signs of vector mean of the observed data: $\bar{\boldsymbol{y}} = [-3.02, 4.32, -5.08]^T$ for Δ(ΔAPD/Δx) and $\bar{\boldsymbol{y}} = [-8.38, 5.38, -1.58]^T$ for Δ(ΔDI/Δx). The relative magnitudes of the posterior probabilities presented in the two tables may also be seen in Figures S1 and S2. Figure S1 shows contour plots of the posterior marginal density functions $p(\mu_1, \mu_2|\boldsymbol{x})$, $p(\mu_2, \mu_3|\boldsymbol{x})$ and $p(\mu_1, \mu_3|\boldsymbol{x})$, where $\boldsymbol{x}$ represents the Δ(ΔAPD/Δx)

data. As expected, in each of the plots, the maximum occurs at the corresponding sample average of the Δ(ΔAPD/Δx) data. For example, the maximum of $p(\mu_1, \mu_2|\boldsymbol{x})$ occurs at $\mu_1 = -3.02$, $\mu_2 = 4.32$ in Figure S1A, consistent with corresponding components in $\bar{\boldsymbol{y}}$. Turning our attention to Figure S1B, we see that nearly the entire probability density function lies in the quadrant corresponding to positive μ_2 and negative μ_3. This is consistent with the Δ(ΔAPD/Δx) probability table, which shows that posterior probabilities of sequences ending in signs other than $+, -$ are very small. We can also use this observation to help interpret Figure S1A, since Figure S1B implies that the posterior probability of μ_3 being positive is small. The upper-right quadrant in Figure S1A, which may be roughly interpreted as the $(+, +, -)$ octant, contains only a small fraction of the probability distribution contained in the upper left quadrant (i.e., the $(-, +, -)$ octant). This is also reflected in the large difference between the probability associated with the $(-, +, -)$ sign sequence (91.14%) and the $(+, +, -)$ sign sequence (5.51%) in the Δ(ΔAPD/Δx) probability table above. The same conclusion may be drawn by examining the upper left and lower left quadrants of Figure S1C.

We can analyze the Δ(ΔDI/Δx) data in a similar manner. Figure S2A shows that the posterior marginal density function is largely confined to the negative μ_1, positive μ_2 quadrant. Figures S2B and C then both show that although most of the distribution is contained in the $(-, +, -)$ octant (i.e., the lower-right quadrant in Figure S2B or the lower-left quadrant in Figure S2C), a substantial portion of the distribution is located in the $(-, +, +)$ octant. This explains the large posterior probability for the $(-, +, -)$ sign sequence in the Δ(ΔDI/Δx) table (82.14%), the smaller but substantial posterior probability associated with the $(-, +, +)$ sign sequence (17.30%), and the much smaller posterior probabilities associated with the remaining sequences.

Effects of Measurement Uncertainties:

There are a number of sources of uncertainty in our study; for example, there was noise in the optical data, and in some cases ERP measurements were unavailable, usually due to an ERP search being interrupted by an arrhythmia. The possible effects of noise on our discordant alternans results are addressed in the Discussion section in the main text. Regarding ERP data, in cases where the uncertainty in our ERP measurements was larger than the typical -0/+2 ms range, we used estimated ERP values, as described in the Methods section in the main text. To test the effects of these ERP estimates on our VF prediction results, we first noted that many of the $\Delta S_n S_{n+1}$ values with unknown or uncertain ERPs were suspected to be in the S or I categories, based on comparisons with similar trials where the ERPs were well-known. Using the logistic regression approach of Gelzer, et al.,[1,2] we recomputed the effect likelihood ratio tests for two extreme cases, one called "S" replacement, where all such $\Delta S_n S_{n+1}$ values were classified as "S" intervals, and a second test, called "I" replacement, where all these values were classified as "I" intervals, and compared these results with those of the default estimation method based on ERP averages. The corresponding p-values are shown in Table S4. Table S4 shows that the significance of the effect of dog varied above and below the significance threshold (p = .05) as the ERP estimation method varied. However, the effect of the model prediction was significant in all three estimation scenarios. Hence, perturbations in the ERP estimation method did not alter our conclusion that a significant association exists between the coupled maps model predictions and VF outcomes.

Table S4. P Values for Effect Likelihood Ratio Tests under Different ERP Estimation Schemes

Method	P value for effect of model prediction	P value for effect of dog
Default	< .0001	.0485
"S" replacement	< .0001	.0633
"I" replacement	.0022	.1249

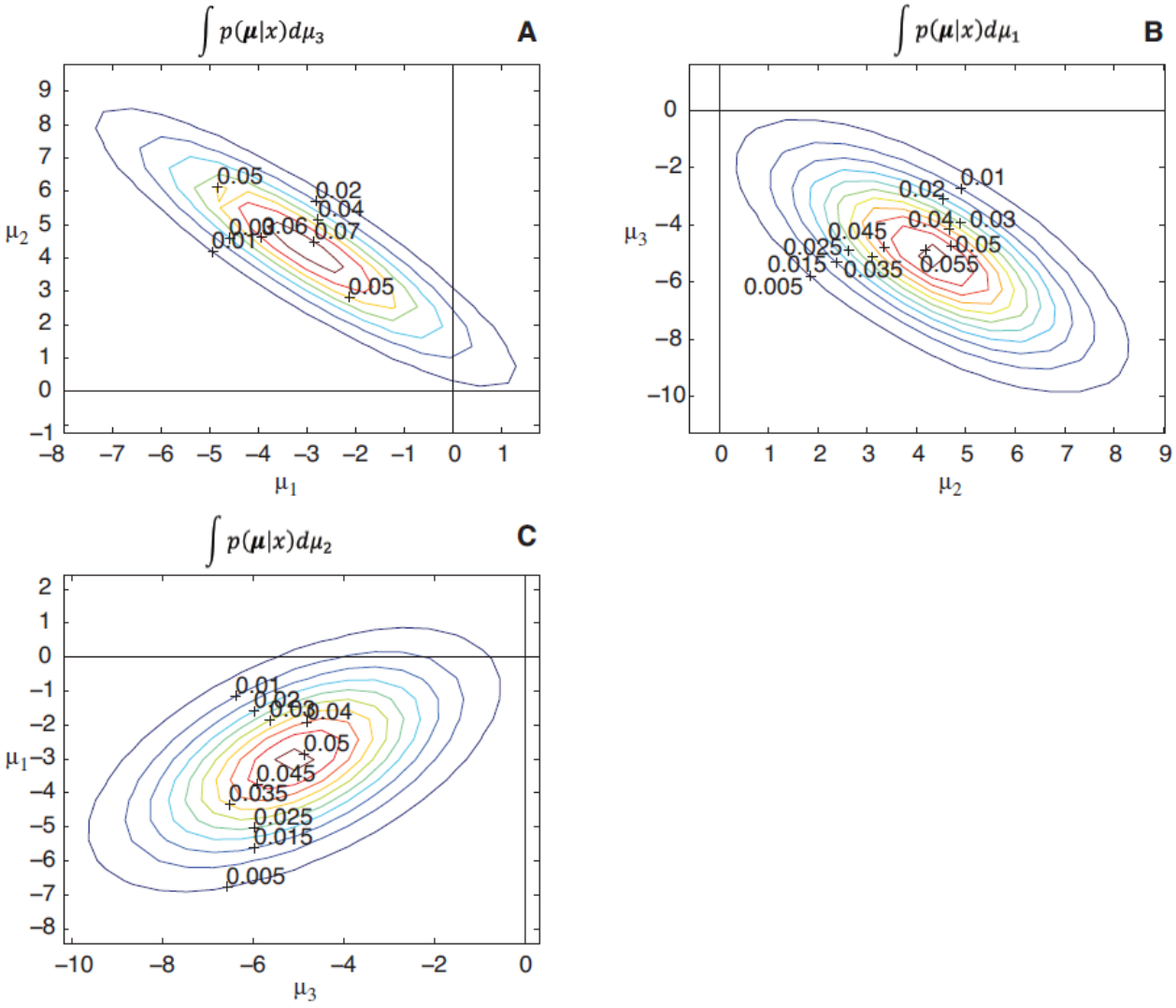

Figure S1. Contour plots of the posterior marginal density functions based on Δ(ΔAPD/Δx) data. A, $p(\mu_1, \mu_2 \mid \boldsymbol{x})$, **B,** $p(\mu_2, \mu_3 \mid \boldsymbol{x})$ and **C,** $p(\mu_1, \mu_3 \mid \boldsymbol{x})$. Vertical and horizontal lines indicate the coordinate axes.

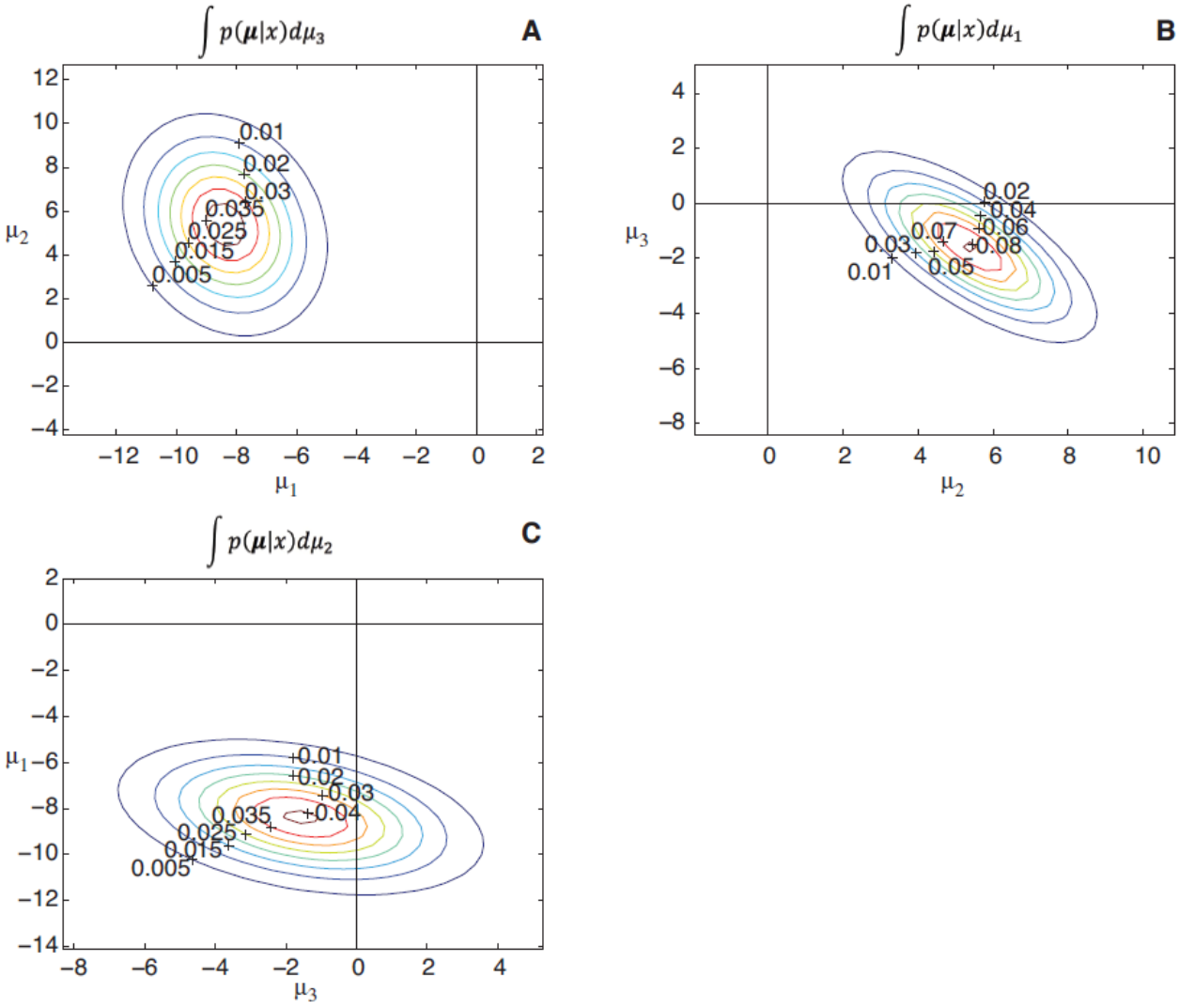

Figure S2. Contour plots of the posterior marginal density functions based on Δ(ΔDI/Δx) data. A, $p(\mu_1, \mu_2 \mid \boldsymbol{x})$, **B,** $p(\mu_2, \mu_3 \mid \boldsymbol{x})$ and **C,** $p(\mu_1, \mu_3 \mid \boldsymbol{x})$. Vertical and horizontal lines indicate the coordinate axes.

Supplemental Movie Legends:

Movies S1-S18 are movies of optical recordings. Movies S1-S4 show the progression of events for the four trials included in Figure 3, and Movies S3 and S5-S18 are the recordings of VF inductions that were used to test the Reentry-Precedes-VF Hypothesis, described in the main text. All movies have the following format: The left panel shows the endocardial surface of the right ventricle, and the right panel shows the epicardial surface. Both panels display normalized membrane potential (dimensionless, 0-10000) over a 128×128 pixel area. The movies have been compressed to accommodate the publisher's size restrictions on individual files; uncompressed movies are available upon request.

Movie S1. Movie of optical data corresponding to Trial NB in Figure 3A, recorded from a test of an SLSL premature stimulus sequence on RV of Dog 4. Sustained VF was not induced. Stimulating electrode tip is located near pixel (50, 100). S_1-S_5 APs become visible at the following times: 122, 296, 442, 572, and 714 ms. Nine spontaneous complexes were observed following S_5, with the first spontaneous complex becoming visible at 886 ms.

Movie S2. Movie of optical data corresponding to Trial 1 in Figure 3B, recorded from a test of an SLSI premature stimulus sequence on RV of Dog 4. Sustained VF was not induced. Stimulating electrode tip is located near pixel (50, 100). S_1-S_5 APs become visible at the following times: 142, 318, 464, 598, and 708 ms. Eight spontaneous complexes were observed following S_5, with the first spontaneous complex becoming visible at 804 ms in the left panel.

Movie S3. Movie of optical data corresponding to Trial VF in Figure 3C, recorded from a test of an SLSI premature stimulus sequence on RV of Dog 4. Sustained VF was induced. Stimulating electrode tip is located near pixel (50, 100). S_1-S_5 APs become visible at the following times: 244, 420, 566, 700, and 798 ms. Spontaneous complexes, followed by VF, were observed following S_5, with the first spontaneous complex becoming visible at 880 ms in the left panel. This instance of VF appeared to have been preceded by reentry.

Movie S4. Movie of optical data corresponding to Trial 2 in Figure 3D, recorded from a test of an SLSI premature stimulus sequence on RV of Dog 9. Sustained VF was not induced. Stimulating electrode tip is located near pixel (40, 80). S_1-S_5 APs become visible at the following times: 188, 394, 564, 730, and 862 ms.

Movie S5. Movie of optical data recorded from a test of an S_1-S_3 premature stimulus sequence on RV of Dog 1. Sustained VF was induced. Based on a review of this movie, it was concluded that S_3 most likely did not capture, resulting in a premature stimulus sequence that was effectively a single "S" interval. Stimulating electrode tip is located near pixel (40, 90). The S_1 and S_2 APs become visible at 150 and 280 ms, respectively. Spontaneous complexes, followed by VF, were observed following S_2, with the first spontaneous complex becoming visible at 408 ms in the left panel. This instance of VF did not

appear to have been preceded by reentry (the initial stages of the arrhythmia appear to involve focal complexes).

Movie S6. Movie of optical data recorded from a test of an SI premature stimulus sequence on RV of Dog 2. Sustained VF was induced. Stimulating electrode tip is located near pixel (70, 100). S_1-S_3 APs become visible at the following times: 122, 310, and 416 ms. Spontaneous complexes, followed by VF, were observed following S_3, with the first spontaneous complex becoming visible at 522 ms in the left panel. This instance of VF appeared to have been preceded by reentry.

Movie S7. Movie of optical data recorded from a test of an SLSI premature stimulus sequence on RV of Dog 2. Sustained VF was induced. Stimulating electrode tip is located near pixel (70, 100). S_1-S_5 APs become visible at the following times: 158, 336, 518, 662, and 760 ms. Spontaneous complexes, followed by VF, were observed following S_5, with the first spontaneous complex becoming visible at 856 ms in the left panel. This instance of VF appeared to have been preceded by reentry.

Movie S8. Movie of optical data recorded from a test of an SS premature stimulus sequence on RV of Dog 3. Sustained VF was induced. Stimulating electrode tip is located near pixel (40, 80). S_1-S_3 APs become visible at the following times: 174, 328, and 414 ms. Spontaneous complexes, followed by VF, were observed following S_3, with the first spontaneous complex becoming visible at 498 ms in the left panel. This instance of VF appeared to have been preceded by reentry.

Movie S9. Movie of optical data recorded from a test of an SLSI premature stimulus sequence on RV of Dog 3. Sustained VF was induced. Stimulating electrode tip is located near pixel (40, 80). S_1-S_5 APs become visible at the following times: 170, 324, 466, 578, and 652 ms. Spontaneous complexes, followed by VF, were observed following S_5, with the first spontaneous complex becoming visible at 726 ms in the left panel. This instance of VF appeared to have been preceded by reentry.

Movie S10. Movie of optical data recorded from a test of an SI premature stimulus sequence on RV of Dog 4. Sustained VF was induced. Stimulating electrode tip is located near pixel (45, 100). S_1-S_3 APs become visible at the following times: 102, 278, and 384 ms. Spontaneous complexes, followed by VF, were observed following S_3, with the first spontaneous complex becoming visible at 482 ms in the left panel. This instance of VF appeared to have been preceded by reentry.

Movie S11. Movie of optical data recorded from a test of an LSI premature stimulus sequence on RV of Dog 4. Sustained VF was induced. Stimulating electrode tip is located near pixel (45, 100). S_1-S_4 APs become visible at the following times: 134, 352, 500, and 606 ms. Spontaneous complexes, followed by VF, were observed following S_4, with the first spontaneous complex becoming visible at 680 ms in the left panel. This instance of VF appeared to have been preceded by reentry.

Movie S12. Movie of optical data recorded from a test of an LLIS premature stimulus sequence on RV of Dog 4. Sustained VF was induced. Stimulating electrode tip is located near pixel (45, 100). S_1-S_5 APs become visible at the following times: 126, 344, 522, 658, and 776 ms. Spontaneous complexes, followed by VF, were observed following S_5, with the first spontaneous complex becoming visible at 864 ms in the left panel. This instance of VF appeared to have been preceded by reentry.

Movie S13. Movie of optical data recorded from a test of an SS premature stimulus sequence on RV of Dog 6. Sustained VF was induced. Stimulating electrode tip is located near pixel (100, 80). S_1-S_3 APs become visible at the following times: 102, 344, and 462 ms. Spontaneous complexes, followed by VF, were observed following S_3, with the first spontaneous complex becoming visible at 558 ms in the left panel. This instance of VF appeared to have been preceded by reentry.

Movie S14. Movie of optical data recorded from a test of an SLSI premature stimulus sequence on RV of Dog 6. Sustained VF was induced. Stimulating electrode tip is located near pixel (100, 80). S_1-S_5 APs become visible at the following times: 120, 288, 430, 556, and 650 ms. Spontaneous complexes, followed by VF, were observed following S_5, with the first spontaneous complex becoming visible at 728 ms in the left panel. This instance of VF appeared to have been preceded by reentry.

Movie S15. Movie of optical data recorded from a test of an SI premature stimulus sequence on RV of Dog 8. Sustained VF was induced. Stimulating electrode tip is located near pixel (70, 105). S_1-S_3 APs become visible at the following times: 126, 318, and 446 ms. Spontaneous complexes, followed by VF, were observed following S_3, with the first spontaneous complex becoming visible at 574 ms in the right panel. This instance of VF appeared to have been preceded by reentry.

Movie S16. Movie of optical data recorded from a test of an SLSI premature stimulus sequence on RV of Dog 8. Sustained VF was induced. Stimulating electrode tip is located near pixel (70, 105). S_1-S_5 APs become visible at the following times: 128, 310, 480, 608, and 708 ms. Spontaneous complexes, followed by VF, were observed following S_5, with the first spontaneous complex becoming visible at 814 ms in the left panel. This instance of VF appeared to have been preceded by reentry.

Movie S17. Movie of optical data recorded from a test of an SI premature stimulus sequence on RV of Dog 9. Sustained VF was induced. Stimulating electrode tip is located near pixel (40, 80). S_1-S_3 APs become visible at the following times: 130, 324, and 460 ms. Spontaneous complexes, followed by VF, were observed following S_3, with the first spontaneous complex becoming visible at 584 ms in the left panel. This instance of VF appeared to have been preceded by reentry.

Movie S18. Movie of optical data recorded from a test of an SLSI premature stimulus sequence on RV of Dog 9. Sustained VF was induced. Stimulating electrode tip is located near pixel (40, 80). S_1-S_5 APs become visible at the following times: 142, 336, 516, 676, and 774 ms. Spontaneous complexes, followed by VF, were observed following S_5, with the first spontaneous complex becoming visible at 904 ms in the left panel. This instance of VF appeared to have been preceded by reentry.

Supplemental References:

1. Gelzer ARM, Koller ML, Otani NF, Fox JJ, Enyeart MW, Hooker GJ, Riccio ML, Bartoli CR, Gilmour, Jr. RF. Dynamic mechanism for initiation of ventricular fibrillation in vivo. *Circulation*. 2008;118:1123-1129.

2. Gelzer ARM, Otani NF, Koller ML, Enyeart MW, Moise NS, Gilmour, Jr. RF. Dynamically-induced spatial dispersion of repolarization and the development of VF in an animal model of sudden death. *Comput Cardiol*. 2009;36:309-312.